Design and Analysis of the SmartWalker, a Mobility Aid for the Elderly

by

Matthew J. Spenko

BS Mechanical Engineering
Northwestern University, June 1999

Submitted to the Department of Mechanical Engineering
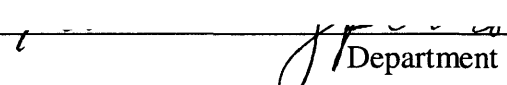in Partial Fulfillment of the Requirements for the Degree of

Master of Science in Mechanical Engineering

at the
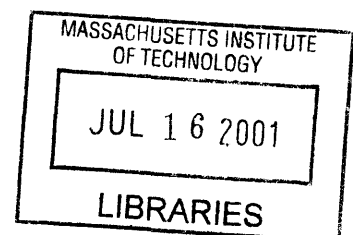
Massachusetts Institute of Technology

June, 2001

Signature of Author_____
Department of Mechanical Engineering
June, 2001

Certified by_____
Steven Dubowsky
Professor of Mechanical Engineering
Thesis Supervisor

Accepted by_____
Ain A. Sonin
Chairman, Departmental Graduate Committee

Design and Analysis of the SmartWalker, a Mobility Aid for the Elderly

by

Matthew J. Spenko

Submitted to the Department of Mechanical Engineering
on June, 2001 in Partial Fulfillment of the
Requirements for the Degree of Master of Science in
Mechanical Engineering

ABSTRACT

In the near future, the baby boomer population will cause a growth in the number of people entering nursing homes. Currently, if people wish to stay out of a nursing home, they must hire a personal aid to take care of daily tasks. A more cost-effective method could be to employ a robotic aid to help with these chores. One such aid is the SmartWalker, a robotic device that would provide health-monitoring sensors, physical support, and help in mobility to the elderly. The focus of this thesis is the design and analysis of the SmartWalker hardware.

The design tools necessary to prevent the SmartWalker from slipping, tipping over, and experiencing brake failure are presented. Furthermore, a study of the omnidirectional platform used on the SmartWalker is performed for uneven terrain. It is shown that all of the wheels of the platform touch the ground at the same time. A simulation of a split caster mobility module, the main component of the omnidirectional platform, traversing a bump is also done. This proves that the control algorithms designed for a perfectly flat floor will suffice on an uneven floor. In addition, this thesis discusses the mechanical design that is necessary to build the SmartWalker. The mechanical design focuses on the split caster mobility modules, the slip rings, the frame, and the tradeoffs between strength and weight.

Thesis Supervisor: Dr. Steven Dubowsky
Title: Professor of Mechanical Engineering

ACKNOWLEDGMENTS

Table of Contents

List of Figures

Chapter

1

<u>Introduction</u>

There are three major contributions of this thesis. The first is the realization of the concept of the SmartWalker, a mobility aid for the elderly (see Figure 1-1).
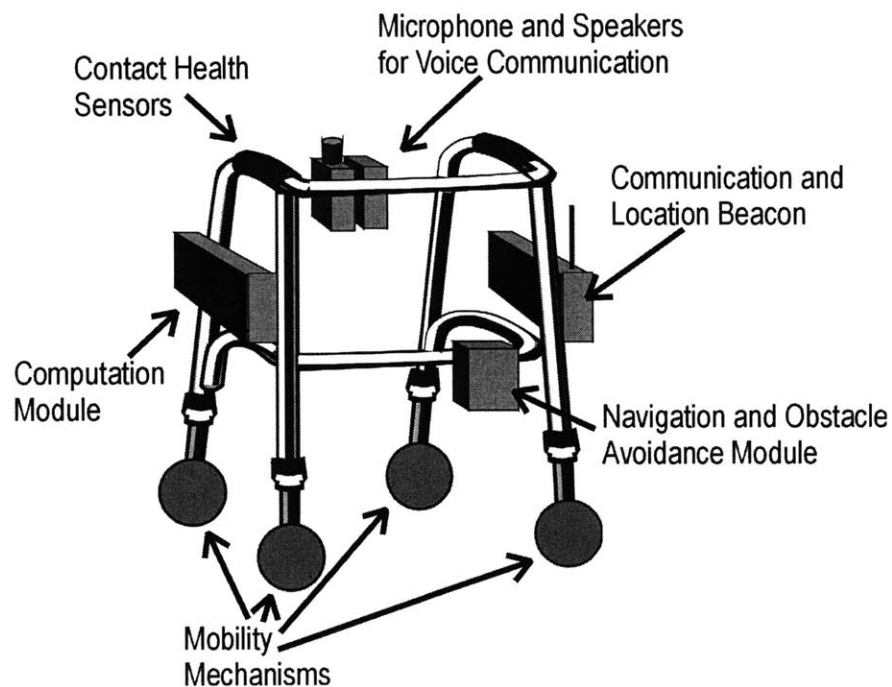
Figure 1-1: SmartWalker Conceptual Drawing (Dubowsky, 2000)

The SmartWalker is comprised of several modules that each perform a separate task. The mobility mechanisms provide the omnidirectional control of the platform. The computation module houses the computer. The communication and location beacon transmits information to and from a central computing facility. The microphone and voice communication module provides an interface between the user and the

SmartWalker. The health sensors acquire data about the user's physical condition. Finally, the navigation and obstacle avoidance module houses sensors that allow the SmartWalker to maintain its course. The second contribution of this thesis is an analysis of the omnidirectional mobility platform used on the SmartWalker. Showing that the omnidirectional platform can be used on an uneven ground and implementing such a device is one of the chief technical challenges of the SmartWalker's design. The last contribution is the results of tests performed on the SmartWalker.

This thesis is divided into six chapters. The first deals with the motivation for the project, background literature, the system concept, and general design issues. The second chapter focuses on the omnidirectional platform used on the SmartWalker. It contains an analysis of the platform's capabilities on an uneven floor. The third chapter discusses the stability of the SmartWalker. This mainly focuses on what forces and conditions would result in the walker slipping, tipping over, or experiencing brake failure. The fourth chapter contains the details of the mechanical design. The fifth chapter shows the results of some of the tests that were performed on the SmartWalker. Finally, the last chapter contains conclusions and ideas for future work in this area.

1.1 Motivation for PAMM

Studies have shown that approximately twenty to thirty-three percent of all nursing home patients do not receive the level and type of care that best serve their needs (Barton, 1997). Furthermore, prolonging the time before an elderly person enters a nursing home can save up to $75,000 a year. Along with the dilemma of increased expenses, many elderly express their desire to not move into nursing homes. With approximately seventy-five million baby boomers about to enter retirement, there is a clear need to develop some way to keep the elderly out of nursing homes for as long as possible (Schneider, 1999).

When elderly people experience a need for help with daily activities, a common occurrence is for them to move into an eldercare facility. These residencies allow their inhabitants to live in their own apartments, but the facility provides meals, health care services, and daily activities. When the elderly encounter such needs as described in

Table 1-1, which currently require the help of a nurse or aid, it is common to move them from the eldercare facility to a nursing home.

Table 1-1: Physical and Cognitive Needs of the Patient (Dubowsky, 2000)

Need	Physical Deficiency	Cause
Guidance	Failing memory, disorientation	Senile dementia, Alzheimer's
Physical support	Muscular/ skeletal frailty, instability	Osteoporosis, Diabetes, Parkinson's Disease, Arthritis, lack of exercise, failure of Vestibular organs
Health monitoring	Poor cardiovascular function, susceptibility to strokes and heart attacks	Poor diet, old age, lack of exercise, illness (e.g. flu or pneumonia)
Medicine or other scheduling	Need to take a variety of medicines coupled with failing memory and disorientation	Senile dementia, general health failure.

Instead of using people to help with these tasks, a class of robotic devices, called PAMM for Personal Aid for Mobility and Monitoring, could be utilized (Dubowsky, 2000). The PAMM systems would provide health-monitoring sensors, physical support, and assistance with mobility. A PAMM system could delay the transition into a nursing home by taking care of the needs of Table 1-1, thus allowing the person to stay at an eldercare facility. One type of a PAMM system is the SmartWalker, whose design and analysis is the focus of this thesis.

1.2 Literature Review

The design of the SmartWalker covers a wide range of topics, and literature exists on each of these. The topics include the following:

- design of conventional walkers for the elderly
- robotic aids for the elderly
- mobility aids for people with various ailments
- omnidirectional wheels and platforms.

Work on conventional walkers is useful for its analysis on stability. The literature on robots that help the elderly describes what other researchers are doing in the field. In addition to robotics for the elderly, there are numerous robots that aid people with other

10

ailments such as blindness. These robots have features that are useful in designing the SmartWalker. Furthermore, the SmartWalker employs an omnidirectional platform for reasons that will be discussed later. The design of such a platform is complex, and knowledge of the numerous current designs along with their advantages and disadvantages is a necessity.

The design of passive walkers has been largely left untreated. There has been some work done concerning stability and the forces that a four-wheeled walker with a seat encounters when a user attempts to rise from a seated position (Finkel, 1997). The work is a good basis for understanding how and why walkers fail to maintain a stable posture.

In recent years there has been a growing interest in the research community to apply robotic technologies to develop intelligent assistive devices for the elderly. The Care-O-bot (see Figure 1-2a) and the Nursebot have been developed for elderly living in private homes (Schraft, 1998; Baltus). The Care-O-bot is intended to be a mobility aid, do household jobs, and provide communication and entertainment functions. This system is in the early stages of development. The Nursebot project focused on studying and enhancing how a robot interacts with a person, including work on human-machine interface methods, tele-presence via the Internet, speech interface, and face tracking. In addition to those two, the PAM-AID (see Figure 1-2b) and the German RoTA are experimental systems developed to aid the visually impaired elderly with mobility (Lacey, 1998; Mori, 1998). None of these projects attempt to deal with the specific issue of providing a comprehensive mobility aid and health-monitoring device for the elderly.
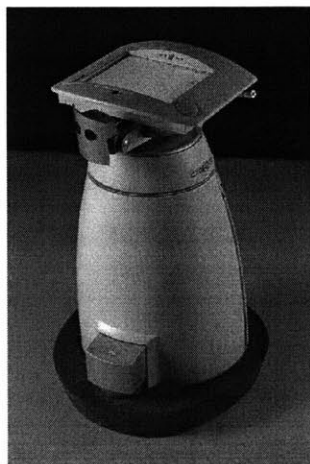
Figure 1-2 (a,b): Care-o-Bot and PAMM-AID (Schraft, 1998; Lacey, 1998)

Other work has focused on the specific problem of mobility in the elderly. The Power-Assisted Walking Support System (see Figure 1-3) is being developed at Hitachi to help support elderly people standing up from bed, walking around, and sitting down (Nemoto, 1998). This device attempts to aid the elderly with all forms of mobility, while the PAMM concept focuses on aiding with ground locomotion only.
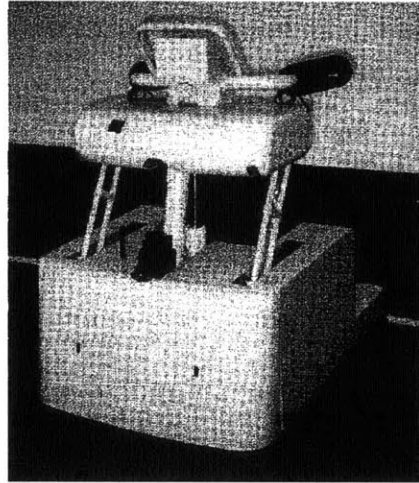
Figure 1-3: Power-Assisted Walking Support System for the Elderly (Nemoto, 1998)

There is another device being developed to assist the elderly in mobility (Miyawaki, 1997). It consists of a powered mobile platform that a user can drive but lacks health-monitoring capabilities or the omnidirectional platform of PAMM.

There has also been substantial work done in the area of robotic wheelchairs. One such wheelchair (see Figure 1-4) has been developed with omnidirectional capabilities (West, 1997). Although this device would be useful for those with severe physical limitations, it is not well suited for the elderly who can still walk. In general, most people use walkers until it is physically impossible for them to walk anymore.

Figure 1-4: Omnidirectional Wheelchair (West, 1997)

One of the main characteristics of the SmartWalker is its omnidirectional platform. Currently there are numerous designs for omnidirectional wheels and platforms (West, 1997; Ferriere, 1998; Muir, 1987; and Yu, 2000). These devices can be divided into two categories, those that employ traditional wheels in unique configurations, and those that use specially designed wheels.

One of the SmartWalker's requirements is that it can be used on a wide range of floors and conditions. It needs to be able to traverse tile, short weave carpet, and in dirty areas. Specialty wheels are usually more complex than conventional wheels, and for that reason they tend to become clogged with dirt more easily. Furthermore, although some specialty wheels could be used on a variety of surfaces, they are too bulky to be incorporated into the SmartWalker. For these reasons, an omnidirectional platform that utilizes conventional wheels is used for the SmartWalker.

Although the aforementioned background work covers a wide variety of subjects, each one of them is necessary for the design of the SmartWalker.

1.3 PAMM System Concept

A conceptual diagram of a generic PAMM system providing support and aiding in the mobility of an elderly user is shown in Figure 1-5. Some of the features of the PAMM system include a 6 axis-force/torque sensor that acts as the input of the user's intentions, a sonar array used to detect obstacles, a vision system that reads signposts on the ceiling to help with localization, health-monitoring sensors, and a way to

13

communicate with a central computer facility. The PAMM's computer and the facility's computer would share such information as navigation routes, the patient's schedule, medical instructions, the patient's location and health status, and any patient requests (Dubowsky, 2000).
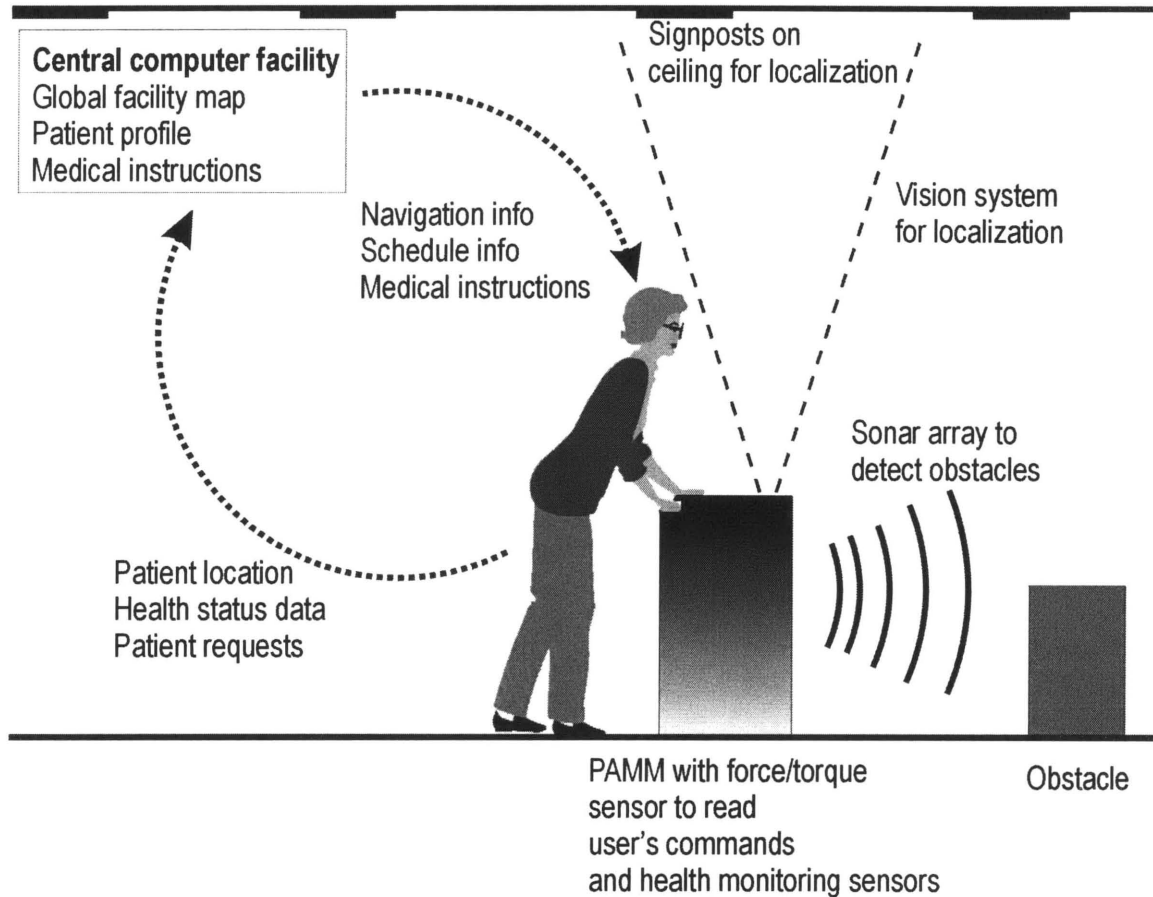
Figure 1-5: PAMM System Concept (Adapted from Dubowsky, 2000)

1.4 First Generation Prototype, the SmartCane

The first implementation of the PAMM system was the SmartCane (Dubowsky, 2000). Its physical design is shown in Figure 1-6. Its main features include a six-axis force/torque sensor to read the user's input, a PC104 based computer system, skid steering, CCD camera for localization, and a sonar array for obstacle detection. Field trials at eldercare facilities were performed to assess the usefulness of the SmartCane (Godding). One of the observations that resulted from these sessions is that some of

people who could benefit from the intelligent features of the PAMM systems need more support than the cane can offer. Thus, the development of the SmartWalker was initiated.

CCD camera

Acoustic
sensor array

6 axis force/torque
sensor

DC/DC
converter

133 Mhz PC104+
DOS based computer

13Wh NiCd
battery x2

Motors with
optical encoders

PC104+
expansion cards
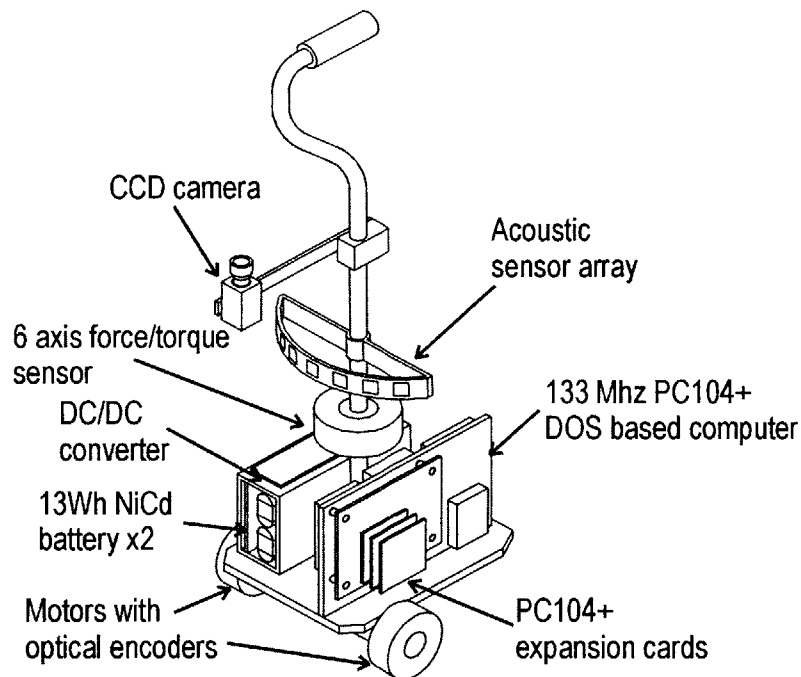
Figure 1-6: Physical Layout of the SmartCane (Dubowsky, 2000)

1.5 Second Generation Features

The SmartWalker uses some of the same features as the SmartCane. The SmartWalker also augments these with a longer battery life, added support, health-monitoring capabilities, and omnidirectional movement.

1.5.1 Battery Life

In order to achieve a longer battery life, the SmartWalker employs pulse-width modulation (PWM) as opposed to linear amplifiers to control the motors (Kozono, 2000). A linear amplifier works by outputting an attenuated source voltage, which results in wasted power. PWM amplifiers work by rapidly switching between allowing all of the voltage through and none at all. This way a PWM amplifier can achieve close to ninety-five percent efficiency compared to the approximately twenty percent of a linear amplifier (Tal, 1976). In addition the PWM amplifier has the added benefit of being smaller and lighter than a linear amplifier.

1.5.2 Added Support

A study by the Center of Disease Control found that 25.2% of the population in nursing homes uses walkers (Gabrel, 2000). Thus, the SmartWalker provides the intelligent features of PAMM to a percentage of the elderly population that requires more support than a cane can furnish.

1.5.3 Health Monitoring Capabilities

The walker also incorporates sensors that monitor a user's pulse. This was not possible on the SmartCane because it only has one handle, and two handles are required. More detailed information about the SmartWalker's health monitoring capabilities can be found in other literature (Darrigo, 2001).

1.5.4 Omnidirectional Platform

The walker is inherently larger and bulkier than a cane. Thus, a skid-steer drive mechanism on the walker would greatly reduce its mobility. To create a system with as much maneuverability as the SmartCane, an omnidirectional mobility platform is needed. The benefits of an omnidirectional system are clear. For example, a user trying to sit in a chair that is directly on his right would easily be able to shuffle to his right using an omnidirectional system. However, if the walker has a skid-steer drive, then the user would need to rotate ninety degrees clockwise, move forward, and then rotate ninety degrees counterclockwise (see Figure 1-7). Therefore, the omnidirectional platform development is vital.
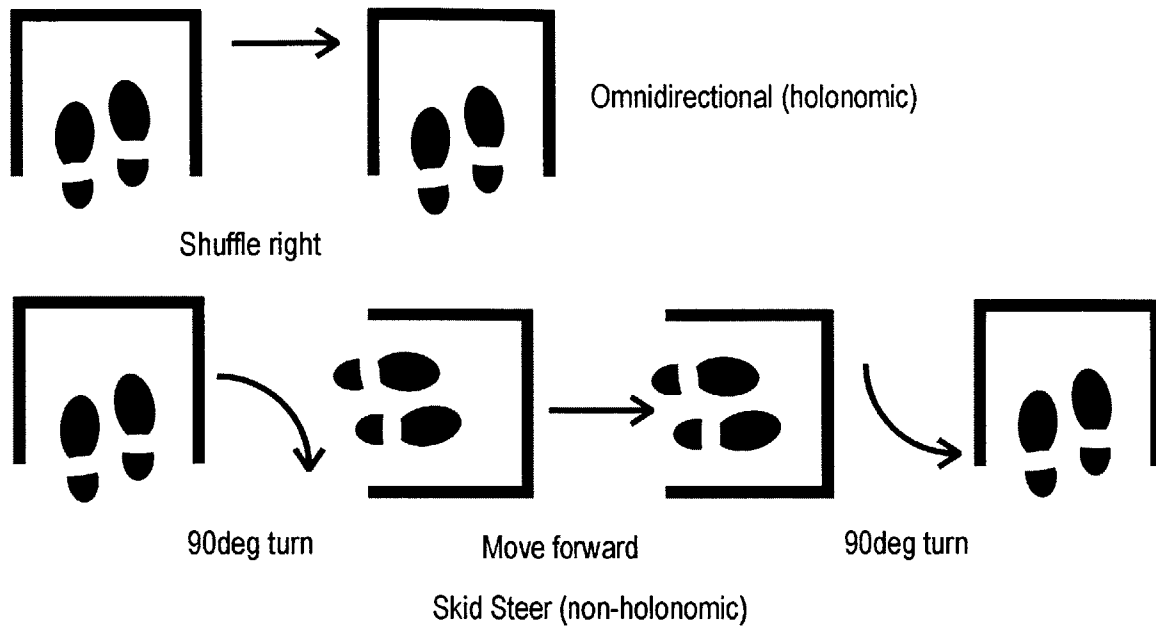
Figure 1-7: Movements Necessary for Holonomic and Non-Holonomic Mobile Platforms

1.6 SmartWalker Design Goals

The first step in designing the SmartWalker was developing a set of design parameters and goals, which along with their justifications are shown in Table 1-2 through Table 1-4.

Table 1-2: Environmental Parameters

Facilities	Indoor
Floor	Tile or thick weave carpet
Ramp	Less than 5 degrees
Light	Normal conditions

Table 1-3: Mechanical Goals

Width	~ Standard walker's width
Length	< 1.5 times a standard walker's length
Height	Adjustable
Weight	Less than 25 kg
Speed	0.4 m/s maximum
Mobility	Omnidirectional
Vertical loading	~ 55 kg
Battery life	One charge per eight hours
Design	Modular so it can be reconfigured
Safety measures	Emergency brake, collision detection, acceleration detection

17

Table 1-4: Communication and Control Goals

Authority	Shared between the user, PAMM, and the central facility computer
Planning and control system	Onboard
Localization	Able to fully locate after each start, frequent enough for accurate motion control
Acoustic obstacle avoidance and recognition	Able to detect and avoid new obstacles at least 4 meters away
Control accuracy	< 15 mm in localization error per 1 m < 10 deg. angular error per 1 m

1.7 Conclusions

This chapter described the concept of the PAMM project as well as early steps in the design of the SmartWalker. The chapter also introduced the SmartCane, the first prototype of a PAMM system. Furthermore, this chapter supplied the background literature necessary to properly design the SmartWalker. Perhaps most importantly, the motivation behind the PAMM project was also presented in this chapter.

Chapter

2

Omnidirectional Platform Design and Analysis

One of the main challenges in this project is the design and implementation of the omnidirectional platform. This chapter details the analysis of such a platform, which is based on a previous design (Yu, 2000). The first part of the chapter shows what the omnidirectional platform looks like and why an analysis needs to be done for uneven surfaces. Why the platform is omnidirectional can be found in other literature (Yu, 2000). The next section of this chapter proves that all the wheels maintain contact with the ground. The third part of the chapter derives the equations of motion for an uneven floor. Finally, the fourth part of this chapter shows the results of a simulation of a split caster mobility module, the basis of the omnidirectional platform, traversing a bump. This simulation demonstrates that the platform's control algorithm, which is designed for a flat surface, will perform adequately on an uneven floor.

2.1 Split Caster Mobility Module Analysis for Uneven Terrain

The type of omnidirectional platform (ODP) that is used on the SmartWalker consists of two split caster mobility modules (SCMM), a bar linking the two together, and at least one additional wheel used for support (Yu, 2000). The four powered wheels make up two split caster mobility modules (see Figure 2-1).
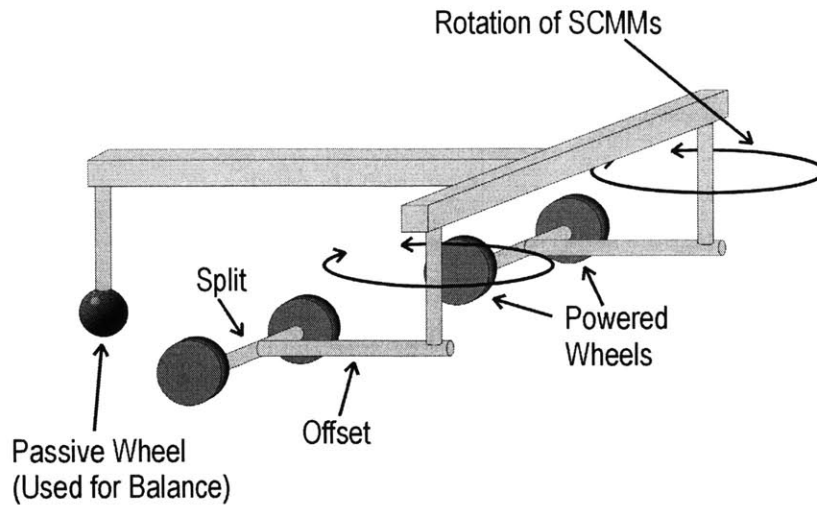
Figure 2-1: General Omnidirectional Platform

In order to ensure that control algorithms will work properly, each of the powered wheels must maintain contact with the floor at all times. If the floor is uneven, then the SCMMs will loose contact with the ground. This is evident by examining Figure 2-2. It shows a two-dimensional image of the omnidirectional platform as if one were looking at it from ground level. In the top part of the figure, the floor is level and there is no problem with the wheels maintaining contact. The bottom part of the figure shows an uneven surface and demonstrates that one of the wheels fails to make contact.
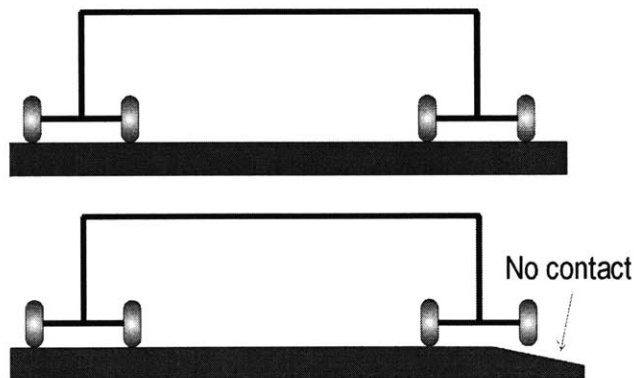
Figure 2-2: Ground Contact of SCMMs on Flat and Uneven Terrain

To overcome this problem, a suspension is added to the wheels. Two possible suspensions, independent and pivot, are shown in Figure 2-3.
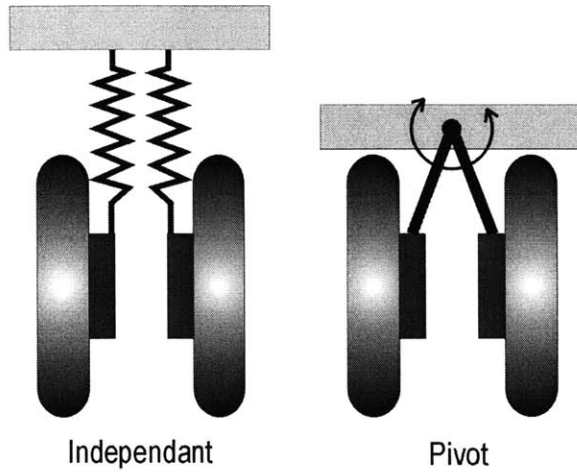
Figure 2-3: Types of Suspension

For simplicity the pivot suspension is used on the SmartWalker. It consists of a passive joint added at point C (see Figure 2-4), and it allows member β, the encoder shaft, to rotate freely about the u-axis.
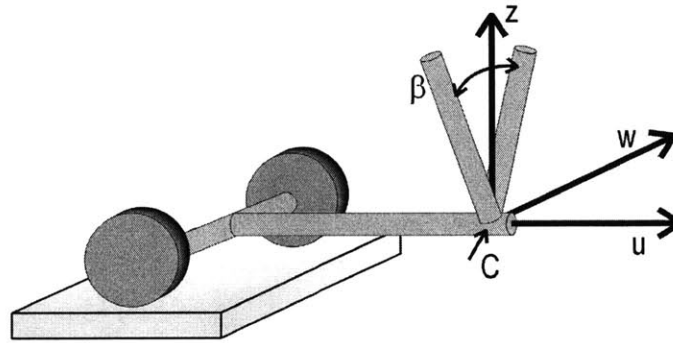
Figure 2-4: Added Joint to SCMM

The arrows in Figure 2-5a show the rotation of the SCMMs now that the pivot joint has been added.
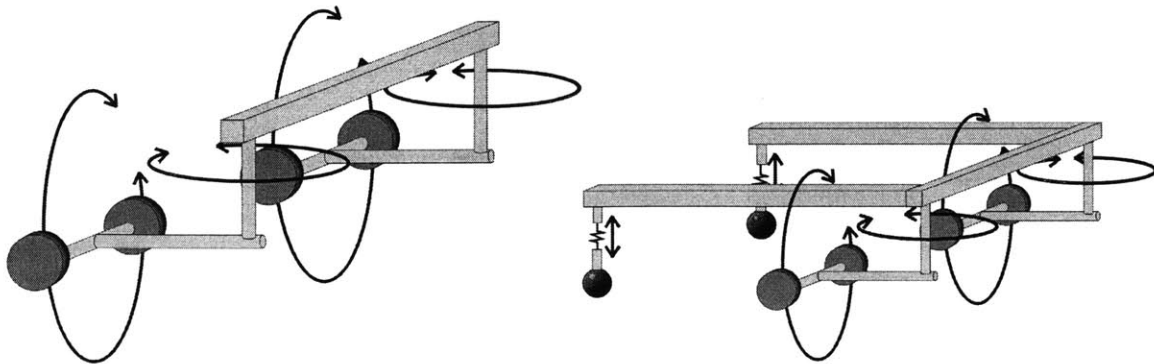
Figure 2-5 (a,b): Minimum Requirements for ODP and Complete ODP

For the SmartWalker, two passive casters with spring suspensions are used in the rear of the platform to maintain stability (see Figure 2-5b).

A closer look at the omnidirectional platform traversing an uneven terrain poses two questions:

1. Is contact with the ground guaranteed at all times?
2. Do the added joints to the system cause any undesirable motions or cause the platform to veer too far off the intended path?

2.2 Proof that All Wheels Touch the Floor at the Same Time

The first question will be answered by showing that all of the wheels of the walker can and do touch the surface of an uneven terrain at the same time. This is done in three steps:

1. It is shown that the two wheels of one SCMM touch the ground.
2. Then, with the first SCMM set in place, it is shown that the configuration space of the second SCMM's wheels lies on the ground.
3. Finally, it is shown that any passive casters can touch the ground if they have independent suspensions.

It is assumed that the wheels are modeled as thin disks. All dimensions are with respect to an inertial reference frame (see Figure 2-6). It must be noted that the two wheel contact points *do not* necessarily lie along a line that is parallel to the axle. However, this analysis is constrained to a slightly uneven floor, and thus it is assumed that the two wheel contact points *do* lie along a line that is parallel to the axis. All the figures in this section represent rough terrain in order to clarify dimensions and make the figures easier to read.
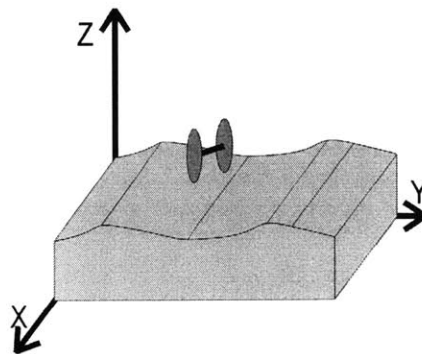
Figure 2-6: Inertial Reference Frame

Given a point on the surface of the ground:

$$P_1(x_1, y_1, z_1)$$ (2-1)

Choose a second point, P_2, to lie in the same plane, $\mathcal{P}_{XZ}$, as P_1, such that P_2 is represented as:

$$P_2(x_2, y_1, z_2)$$ (2-2)

With the constraint that

$$d = \sqrt{(x_2 - x_1)^2 + (z_2 - z_1)^2}$$ (2-3)

where d is the length between the two wheels (see Figure 2-7).
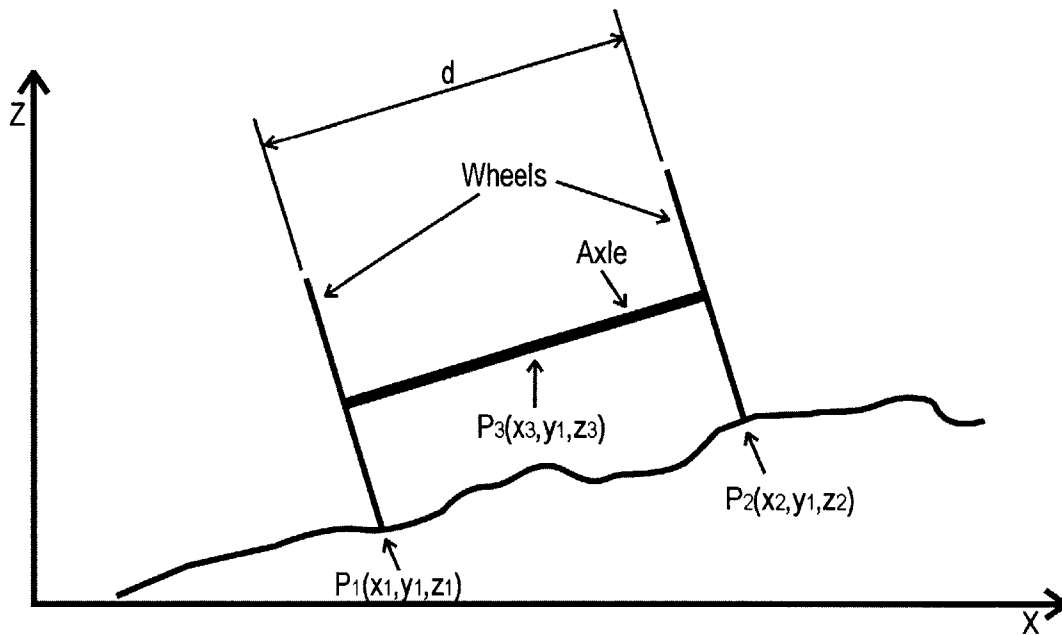
Figure 2-7: SCMM on Uneven Terrain

Inside the x-curve, the curve of intersection of $z = f(x, y)$ with a vertical plane parallel to the xz-plane, y_1 can be taken to be a constant, such that the ground can be represented by $z = f(x)$ (Edwards, 1994). Given x_1 and the function that represents the height of the ground,

$$z = f(x)$$ (2-4)

it is possible to find z_1. Knowing x_1 and z_1 and utilizing Equations (2-3) and (2-4) it is possible to determine the location of point P_2. If the two points P_1 and P_2 can exist on the x-curve, then the point $P_3(x_3, b, z_3)$, which is the location of the joint in the SCMM, also exists (see Figure 2-7).

23

If the wheels of the SCMM are fixed in space and the point P_3 is shifted along the Y-axis by a distance s, the offset length of the SCMM, then the position of point C (see Figure 2-8) is determined. Using the equation of a sphere it can be shown that from point P_3, the configuration space of the point $P_3'(x_3', y_3', z_3')$, the point on the second SCMM corresponding to P_3, is bounded by the following inequality:

$$(h-s)^2 \leq (x_3' - x_3)^2 + (y_3' - (y_1 + s))^2 + (z_3' - z_3)^2 \leq (h+s)^2 \qquad (2\text{-}5)$$

where h is the length of the bar that attaches the two SCMMs.
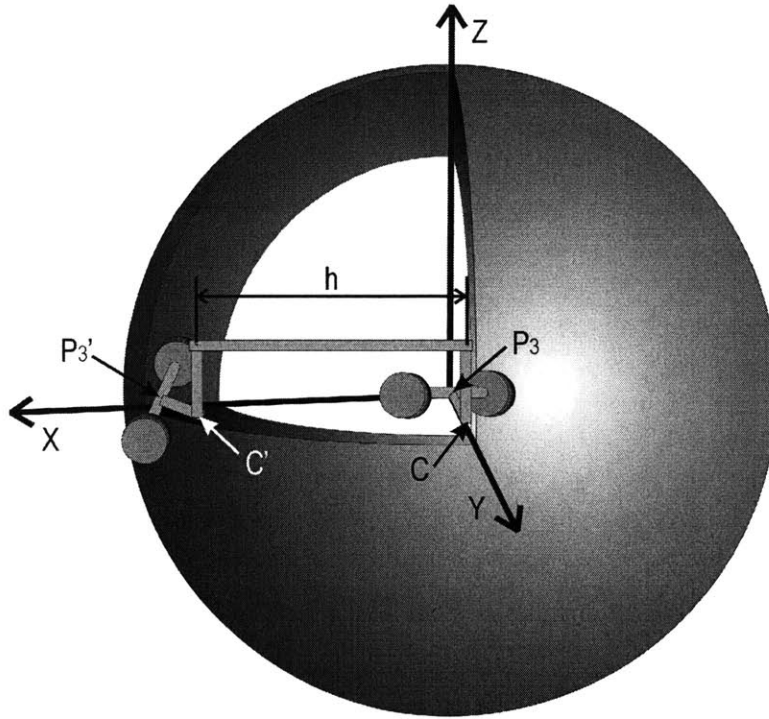
Figure 2-8: Configuration Space of the Second SCMM

This can be compared to the configuration space of a platform had it not contained any joints, which is defined by the following inequality:

$$(h-s)^2 \leq (x_3' - x_3)^2 + (y_3' - (y_1' + s))^2 \leq (h+s)^2 \qquad (2\text{-}6)$$

This is shown graphically in Figure 2-9.
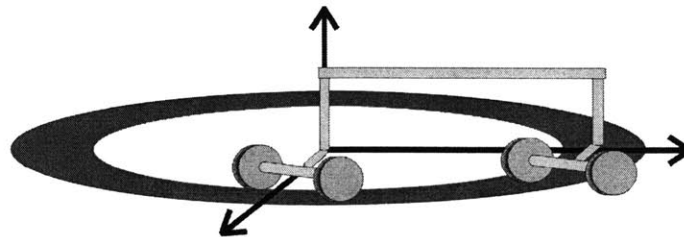
Figure 2-9: Configuration Space of Second SCMM without Added Joint

24

As one can see, the configuration space for the SCMM without the suspension lies in a plane, while the configuration space for the design with the suspension lies within a sphere. As long as the terrain exists inside of the configuration space, which is true for all cases except when the terrain is a sphere with a radius less than (h+s), then the point P_3' can exist at any height above the terrain. If that is the case, then the two points P_1' and P_2' can also exist. This is possible because given P_1, it is possible to find P_2 and P_3. Applying the converse, given P_3' it is possible to find P_1' and P_2'. Thus, all four wheels of the two SCMMs can touch the ground at the same time on an uneven terrain.

This is easily shown graphically for the simple case of points P_3 and P_3' lying in the same x-curve, such that $y_1 = y_1'$. This is equivalent to reducing the configuration space to a circle of radius h. This is shown in Figure 2-10. Obviously the terrain on the right would be unreasonable for the SmartWalker, but nonetheless it exemplifies the proof.
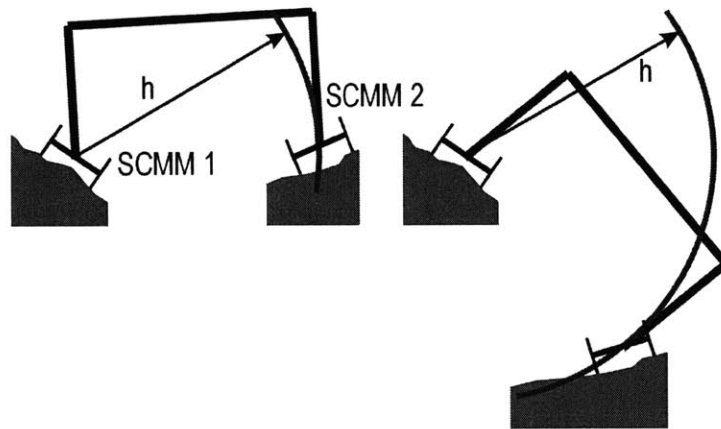
Figure 2-10: ODP in Various Degrees of Uneven Terrain

There are a few restrictions for the analysis to hold true. It is necessary to make sure that the terrain does not interfere with the axle of the SCMM as shown in Figure 2-11.

Figure 2-11: Ground that is too Rough for SCMM

This is accomplished by imposing the following constraints on the function that describes the ground, z = f(x). Note that these constraints are only valid for the general case where the axle is a considered a thin line. Actual designs of the SCMMs would naturally require the axle to have a certain diameter and have additional material to hold the axle bearings. This would require modifications on this general case.
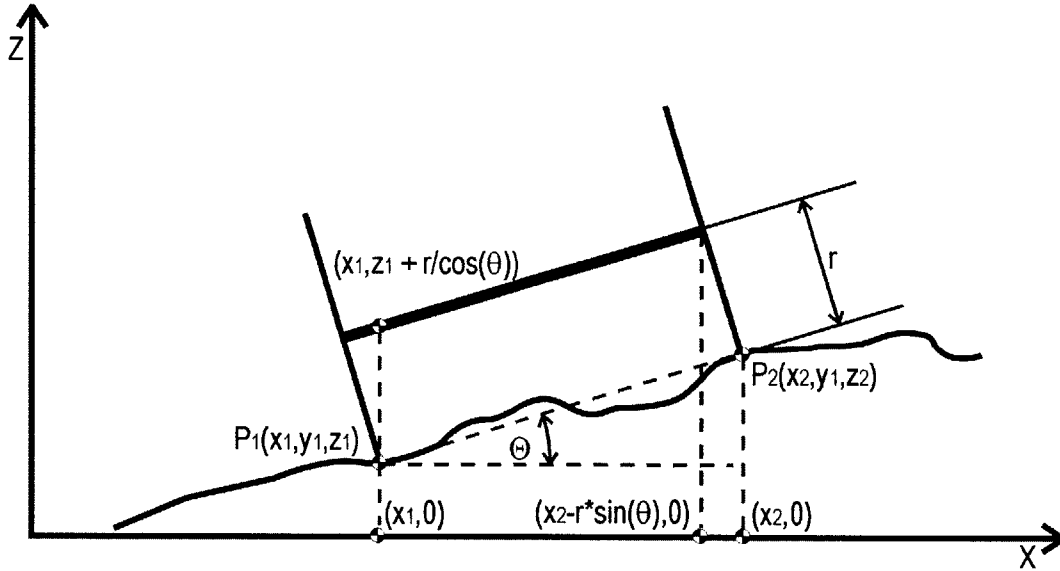
Figure 2-12: SCMM Notation

For the case where $\theta > 0$ (see Figure 2-12):

$$z \leq \tan\theta\left(x\text{-}x_1 + \frac{r}{\sin\theta}\right) + z_1 \quad \text{for}\left\{x_1 < x < x_2\text{-}r\sin\theta\right\} \tag{2-7}$$

$$z < -\cot\theta\left(x - x_2\right) + z_2 \quad \text{for}\left\{x_2\text{-}r\sin\theta < x < x_2\right\} \tag{2-8}$$

For the case where $\theta < 0$:

$$z \leq \cot\theta\left(x - x_1\right) + z_1 \quad \text{for}\left\{x_1 < x < x_1 + r\sin\theta\right\} \tag{2-9}$$

$$z < -\tan\theta\left(x - x_2\right) + z_2 - \frac{r}{\cos\theta} \quad \text{for}\left\{x_1 + r\sin\theta < x < x_2\right\} \tag{2-10}$$

It is assumed that any additional passive casters belong to the same plane as the SCMMs. The coordinates of passive caster i are (u_i, v_i, w_o+l_i) where u_i and v_i are static values that are related to the geometry of the ODP, w_o is some nominal value related to the ODP's frame, and l_i is the extension of the spring (Simeon, 1993). This shows that the passive casters can also maintain contact with an uneven floor. Thus, all of the wheels of the ODP touch the ground at all times.

2.3 Analysis of the Control System Designed for a Flat Floor Applied to an Uneven Floor

This section derives the equation that describes the velocity of a SCMM traversing an uneven floor in three dimensions. A simulation is done to show that a SCMM running over a bump in the floor will not significantly deviate from the desired path.

The base plane, $\mathcal{P}_{base}$, is considered to be the "flat floor" and is defined by $z = 0$, where the gravity vector $\mathbf{n} = [0,0,-1]^T$ is normal to $\mathcal{P}_{base}$. The encoder shaft (the shaft between points C and D in Figure 2-13) of the SCMM is assumed to always be normal to $\mathcal{P}_{base}$. This ensures that $\mathbf{n}_{EncoderShaft} = [0,0,1]$. As shown in Figure 2-10, this statement is not always true, but the assumption can be made for relatively flat surfaces.
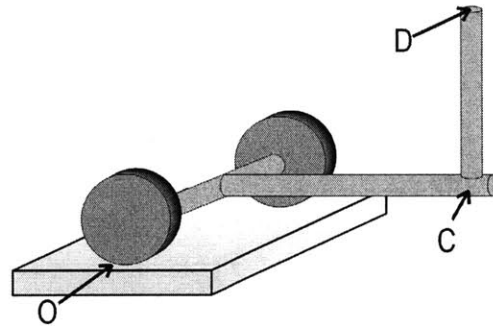
Figure 2-13: Notation of Various Points on the SCMM

A few other dimensions must be defined (see Figure 2-14). The angle θ is the amount that the SCMM is tilted about the u-axis. Angles γ_1 and γ_2 are the contact angles of the ground at each wheel respectively. The dimension s is the length of the offset and d is the length of the split. Ψ is the angle of the SCMM with respect to the X-axis.
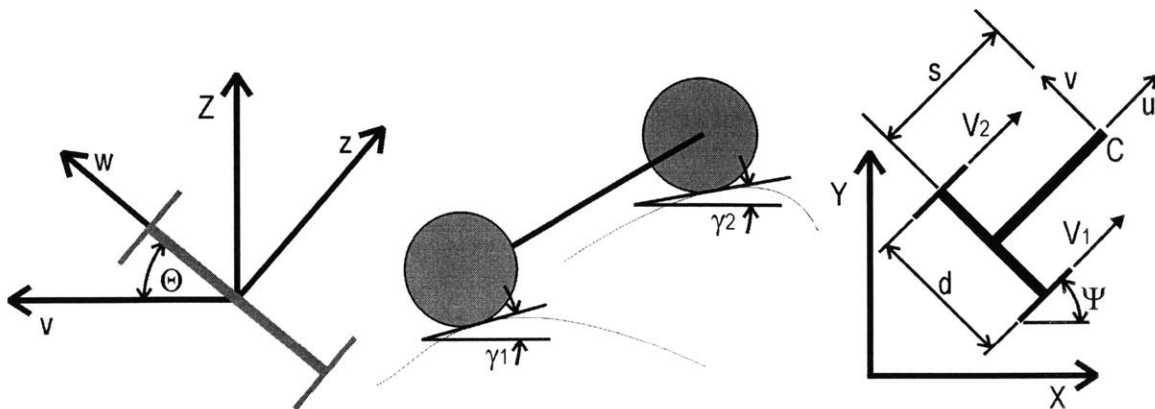
Figure 2-14: Explanation of Various Dimensions

The velocity of point C for the two-dimensional case is given as:

$$_{\alpha}\mathbf{V}_C = \frac{1}{2}(V_1 + V_2)\mathbf{u} + \frac{s}{d}(V_1 - V_2)\mathbf{v}$$ (2-11)

where **u** and **v** are unit vectors shown in the right side of Figure 2-14 (Yu, 2000). The same equation, translated into the inertial frame is given as:

$$\begin{bmatrix} V_X \\ V_Y \end{bmatrix} = \begin{bmatrix} \frac{1}{2}(V_1 + V_2)(\cos\Psi) - \sin\Psi\left(\frac{s}{d}(V_1 - V_2)\right) \\ \frac{1}{2}(V_1 + V_2)(\sin\Psi) + \cos\Psi\left(\frac{s}{d}(V_1 - V_2)\right) \end{bmatrix}$$ (2-12)

For the three-dimensional case, the velocity of point D needs to be determined (see Figure 2-13). The velocity of point D is given by:

$$_{\alpha}\mathbf{V}_{D/_O} = {_{\alpha}\mathbf{V}_{D/_C}} + {_{\alpha}\mathbf{V}_{C/_O}}$$ (2-13)

where the α-frame is the ground (inertial frame). For a given V_1 and V_2, the respective velocities of each of the wheels, the velocity of point C in the three-dimensional case is:

$$_{\alpha}\mathbf{V}_{C/_O} = \left[\frac{1}{2}(V_1\cos\gamma_1 + V_2\cos\gamma_2)\right]\mathbf{u} + \left[\frac{s}{d}(V_1 - V_2)\right]\mathbf{w} + \left[\frac{1}{2}(V_1\sin\gamma_1 + V_2\sin\gamma_2)\right]\mathbf{z}$$

(2-14)

where **u**, **w**, and **z** are unit vectors shown both in Figure 2-4 and Figure 2-14. Note that **u**, **w**, and **z** do *not* constitute an inertial frame. It is a body-fixed frame that has its origin at point C. Thus, Equation (2-14) is an extension of (2-11). V_1 and V_2 from the first term are replaced with the components $V_1\cos(\gamma_1)$ and $V_2\cos(\gamma_2)$, and two terms are added in the z-direction (see Figure 2-15).
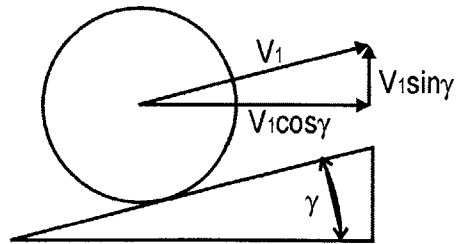
Figure 2-15: Explanation of Notation

Now to solve (2-13), only $_{\alpha}\mathbf{V}_{D/_C}$ needs to be obtained. As the floor becomes uneven, the joint rotates an angle of θ and with an angular velocity of $\dot{\Theta}$.

Thus,

$$\alpha \mathbf{V}_{D/C} = \beta \mathbf{V}_{D/C} + \alpha \mathbf{\Omega}_\beta \times \mathbf{r}_{D/C}$$

$$\alpha \mathbf{V}_{D/C} = 0 + \det \begin{vmatrix} \mathbf{u} & \mathbf{w} & \mathbf{z} \\ \dot{\Theta} & 0 & 0 \\ 0 & -l\sin\Theta & l\cos\Theta \end{vmatrix} \tag{2-15}$$

$$\alpha \mathbf{V}_{D/C} = \left[-\dot{\Theta}l\cos\Theta\right]\mathbf{w} - \left[\dot{\Theta}l\sin\Theta\right]\mathbf{z}$$

where l is the distance from point C to point D. Therefore,

$$\alpha \mathbf{V}_D = \left(\frac{1}{2}\left(V_1\cos\gamma_1 + V_2\cos\gamma_2\right)\right)\mathbf{u} + \left(\frac{s}{d}\left(V_1 - V_2\right) - \dot{\Theta}l\cos\Theta\right)\mathbf{w} + $$
$$\left(\left(\frac{1}{2}\left(V_1\cos\gamma_1 + V_2\cos\gamma_2\right)\right) - \left(\dot{\Theta}l\sin\Theta\right)\right)\mathbf{z} \tag{2-16}$$

αV_D is the velocity of point D as observed from the ground, which is an inertial reference frame. Since the flat ground is in terms of coordinates **X**, **Y**, **Z**, not **u**, **w**, **z**, a coordinate transformation must take place in accordance with the convention of Euler's angles. In other words, $[V]_{uwz} = G_\Theta G_\Psi [V]_{XYZ}$ needs to be calculated (see Figure 2-16).
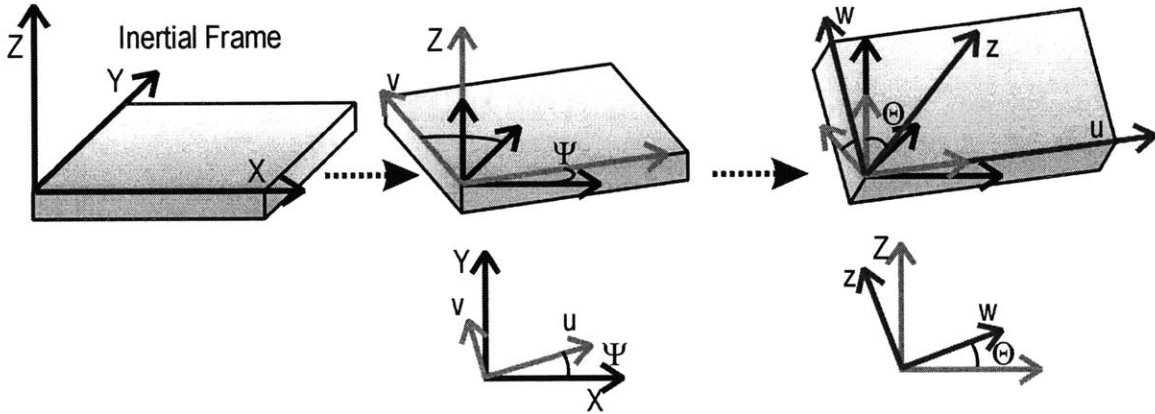
Figure 2-16: Euler's Angles

Where

$$G_\Psi = \begin{bmatrix} \cos\Psi & \sin\Psi & 0 \\ -\sin\Psi & \cos\Psi & 0 \\ 0 & 0 & 1 \end{bmatrix} \text{ and } G_\Theta = \begin{bmatrix} 1 & 0 & 0 \\ 0 & \cos\Theta & \sin\Theta \\ 0 & -\sin\Theta & \cos\Theta \end{bmatrix} \tag{2-17}$$

Thus,

$$G = G_\Theta G_\Psi = \begin{bmatrix} \cos\Psi & \sin\Psi & 0 \\ -\cos\Theta\sin\Psi & \cos\Theta\cos\Psi & \sin\Theta \\ \sin\Theta\sin\Psi & -\sin\Theta\cos\Psi & \cos\Theta \end{bmatrix} \tag{2-18}$$

and

$$G^{-1} = \begin{bmatrix} \cos\Psi & -\cos\Theta\sin\Psi & \sin\Theta\sin\Psi \\ \sin\Psi & \cos\Theta\cos\Psi & -\sin\Theta\cos\Psi \\ 0 & \sin\Theta & \cos\Theta \end{bmatrix} \tag{2-19}$$

Thus,

$$\begin{bmatrix} V_X \\ V_Y \\ V_Z \end{bmatrix} = G^{-1}{}_a V_D = \begin{bmatrix} \cos\Psi & -\cos\Theta\sin\Psi & \sin\Theta\sin\Psi \\ \sin\Psi & \cos\Theta\cos\Psi & -\sin\Theta\cos\Psi \\ 0 & \sin\Theta & \cos\Theta \end{bmatrix} \begin{bmatrix} \frac{1}{2}(V_1\cos\gamma_1 + V_2\cos\gamma_2) \\ \frac{s}{d}(V_1 - V_2) - \dot\Theta l\cos\Theta \\ \frac{1}{2}(V_1\sin\gamma_1 + V_2\sin\gamma_2) - \dot\Theta l\sin\Theta \end{bmatrix}$$

$$= \begin{bmatrix} \left(\frac{1}{2}(V_1\cos\gamma_1 + V_2\cos\gamma_2)\cos\Psi \\ + \sin\Psi\left(\dot\Theta l(\cos^2\Theta - \sin^2\Theta)\frac{s}{d} + \frac{1}{2}(V_1\sin\gamma_1 + V_2\sin\gamma_2)\sin\Theta - \frac{s}{d}\cos\Theta(V_1 - V_2) \right) \right) \\ \left(\frac{1}{2}(V_1\cos\gamma_1 + V_2\cos\gamma_2)\sin\Psi \\ -\cos\Psi\left(\dot\Theta l(\cos^2\Theta - \sin^2\Theta)\frac{s}{d} + \frac{1}{2}(V_1\sin\gamma_1 + V_2\sin\gamma_2)\sin\Theta - \frac{s}{d}\cos\Theta(V_1 - V_2) \right) \right) \\ \left(\frac{1}{2}(V_1\sin\gamma_1 + V_2\sin\gamma_2)\cos\Theta + \sin\Theta\left(\frac{s}{d}(V_1 - V_2) - 2\dot\Theta l\cos\Theta \right) \right) \end{bmatrix}$$

$$\tag{2-20}$$

It can be shown that for θ, γ, and $\dot\Theta$ equal to zero, Equation (2-20) simplifies to

$$\begin{bmatrix} V_X \\ V_Y \\ V_Z \end{bmatrix} = \begin{bmatrix} \frac{1}{2}(V_1 + V_2)(\cos\Psi) - \sin\Psi\left(\frac{s}{d}(V_1 - V_2) \right) \\ \frac{1}{2}(V_1 + V_2)(\sin\Psi) + \cos\Psi\left(\frac{s}{d}(V_1 - V_2) \right) \\ 0 \end{bmatrix} \tag{2-21}$$

which is the equation that was derived for the flat ground (see Equation (2-12)).

30

Given Equation (2-20) it is possible to determine the maximum error in velocity. This is done by comparing the velocity found in Equation (2-20) with that found in Equation (2-21). Equation (2-20) has five unknown variables, γ_1, γ_2, θ, $\dot{\theta}$, and ψ, and the maximum error in velocity results from some combination of those variables. A brute force search for the maximum error in velocity performed with the following values:

$$-5 < \gamma_1, \gamma_2, \theta < 5$$
$$-0.03 < \dot{\theta} < 0.03 \quad\quad\quad (2\text{-}22)$$
$$0 \le \psi < 360$$

where the values for the angles are in degrees and the values for $\dot{\theta}$ are in rad/sec, yields an error in the X-direction of 3.39%. These particular values were chosen since they represent the maximum values that the SCMM might encounter on a typical floor.

2.4 Simulation Parameters

To test whether or not the added joint causes problems with the position of the walker, a simulation of a SCMM running over a bump in the floor was done. The bump was created (see Figure 2-17) using the function:

$$f(x, y) = amp * \exp\left(-\left(peak * x\right)^2 - \left(peak * y\right)^2\right) \quad\quad\quad (2\text{-}23)$$

where *amp* is the height of the bump in meters and *peak* is the sharpness of the bump (no units). Note that the Z-direction is greatly exaggerated in order to better exemplify the shape of the bump.
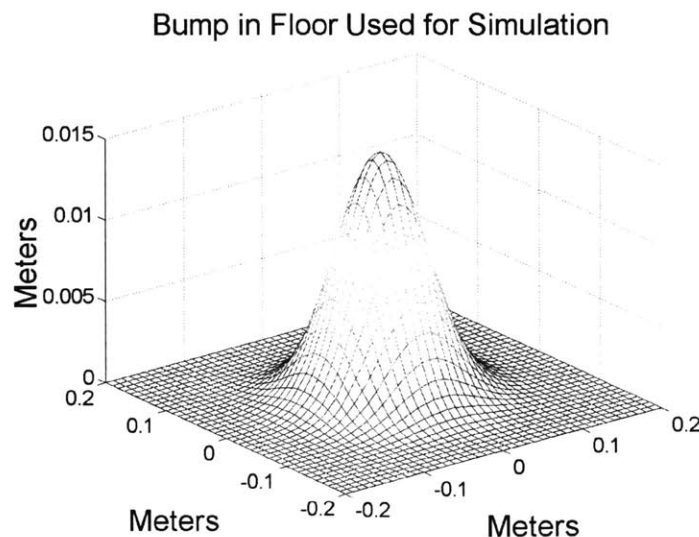
Figure 2-17: Bump Used for Simulation

2.4.1 Simulation Program Structure

The simulation program structure is shown below. Refer to Appendix A for details.
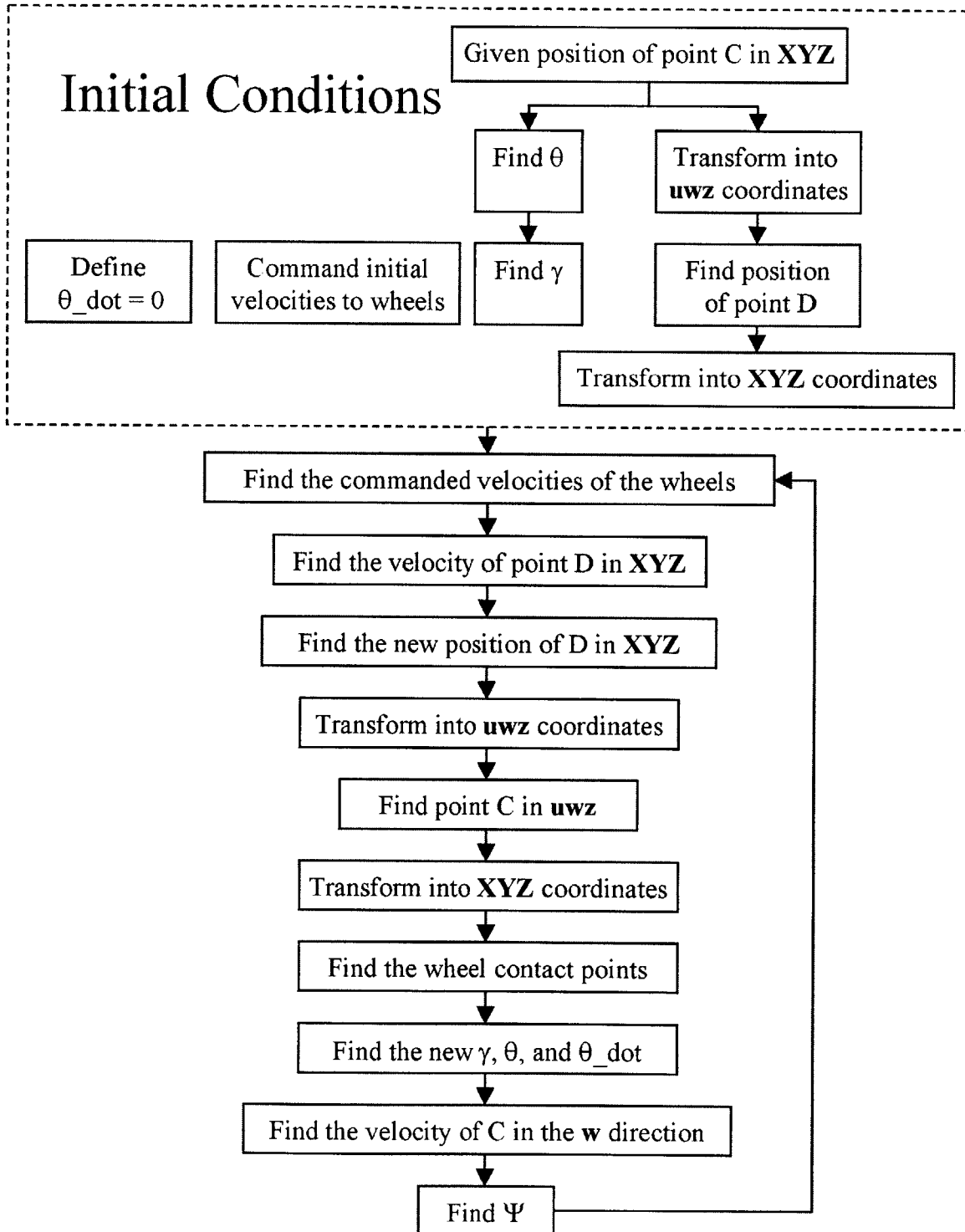
Figure 2-18: Diagram of Simulation Program Structure

2.4.2 Simulation Results

The figures shown below are for a 15 mm high bump with a peak value of fifteen. As the peak value is increased the bump becomes sharper. It is determined that this peak value offers a reasonably shaped bump. The length of the offset, s, is 35.875 mm, the length of the split, d, is 95 mm, the height from the SCMM to the walker frame is 180 mm, and the diameter of the wheels is 76 mm. This bump is about five times as large as what may be found on a typical floor, but the larger bump more clearly exemplifies what can happen to the position of point D. The two lines traversing the floor are the wheel contact points. The single dashed line above the floor is the position of point D.
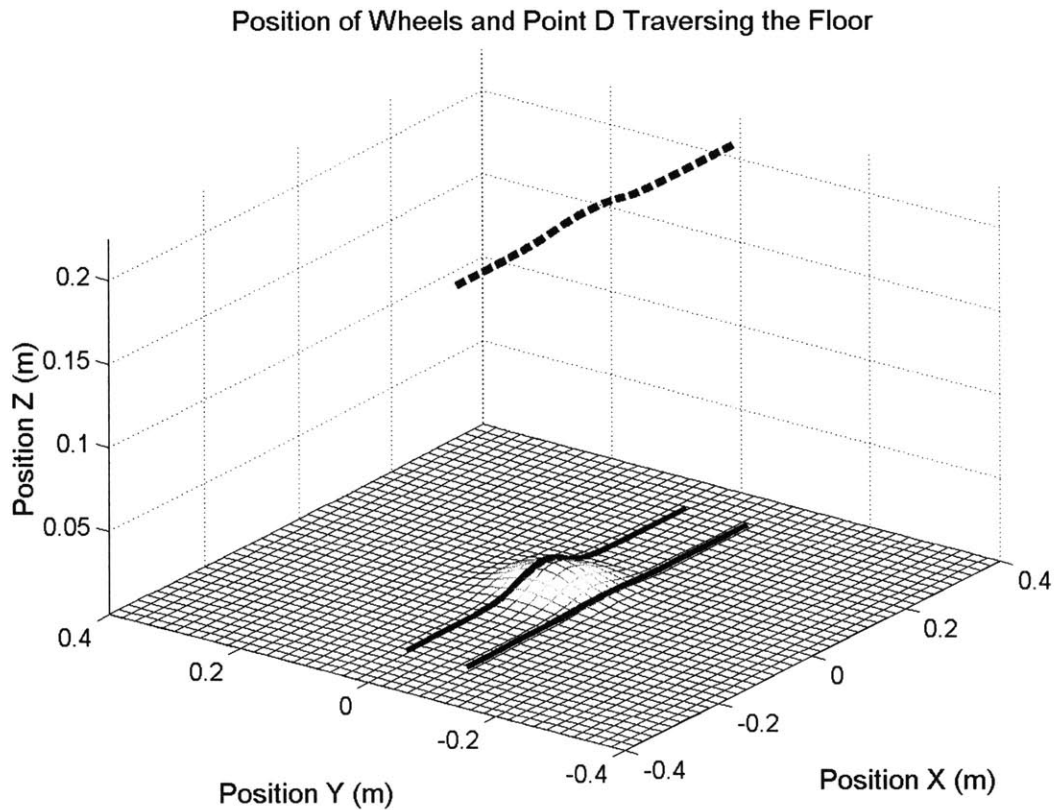
Figure 2-19: Three Dimensional View of the Position of the Wheels and Point D
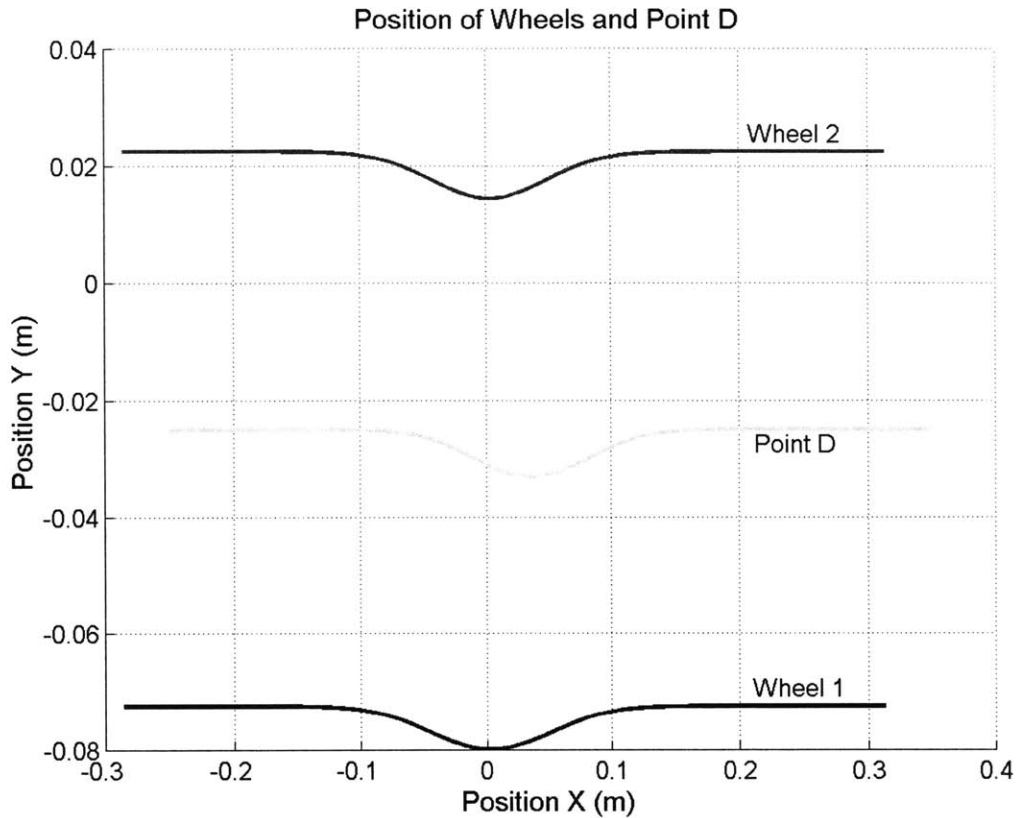
Figure 2-20: Top Down View of the Position of the Wheels and Point D

A top down view of the same path is shown in Figure 2-20 where the lower and upper lines indicate the paths of wheels one and two respectively, and the line in the middle indicates the path of point D.

As one can see, the path of point D deviates from a straight line. However, the controller only dictates that the velocity of point D maintains a speed of 0.2 m/s in the X-direction and zero in the Y-direction; it cannot directly control the position of point D. Figure 2-21 shows the velocity of point D in all three directions. Note that the bump peaks at just under 1.5 seconds.
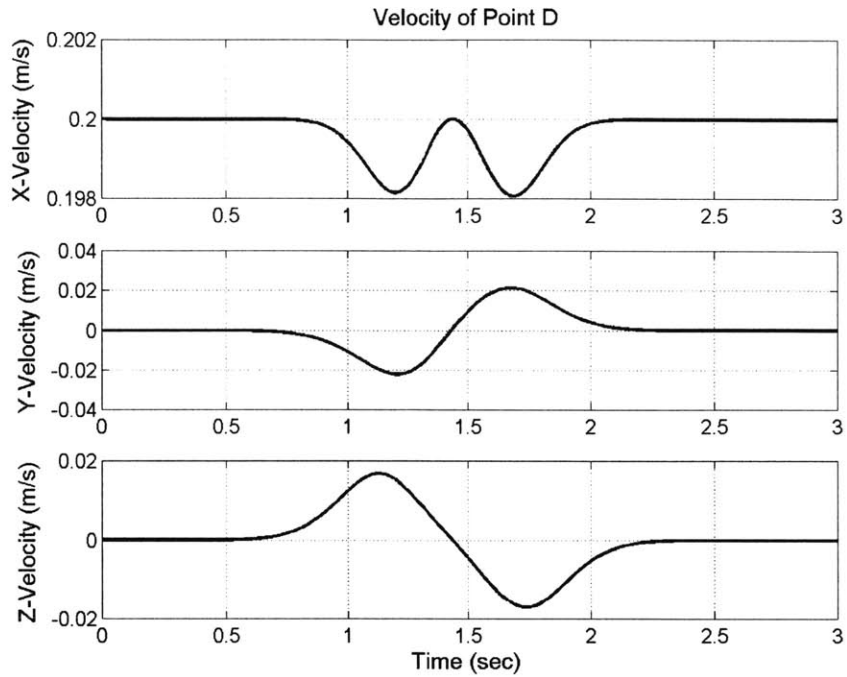
Figure 2-21: Velocity of Point D

Lastly, Figure 2-22 shows the velocity of each of the wheels. Note that the bump causes the encoder shaft to rotate, which in turn causes the controller to modify the velocities of the wheels.
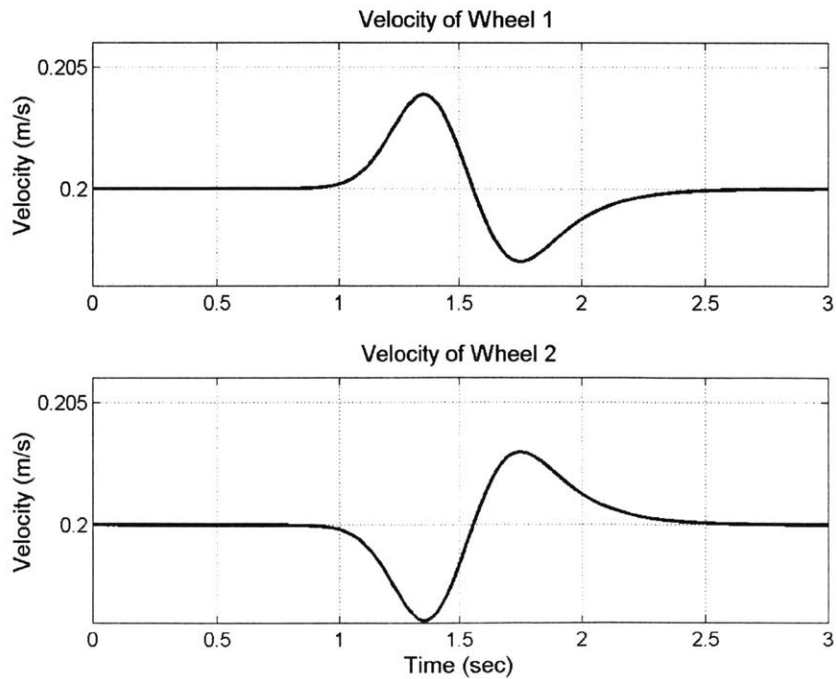
Figure 2-22: Velocity of Wheels One and Two

The deviation of point D from the desired path was found for bump sizes ranging from 0 to 40 mm with a peak of fifteen (no units) (see Figure 2-23). Measurements of a typical tiled floor indicate that a reasonable bump height is about 3 mm. The simulation was run for much higher values to show the non-linearity of the system. The results show that point D would only deviate from its intended path on the order of a few millimeters, which indicates that the control algorithms are sufficient for an uneven floor.
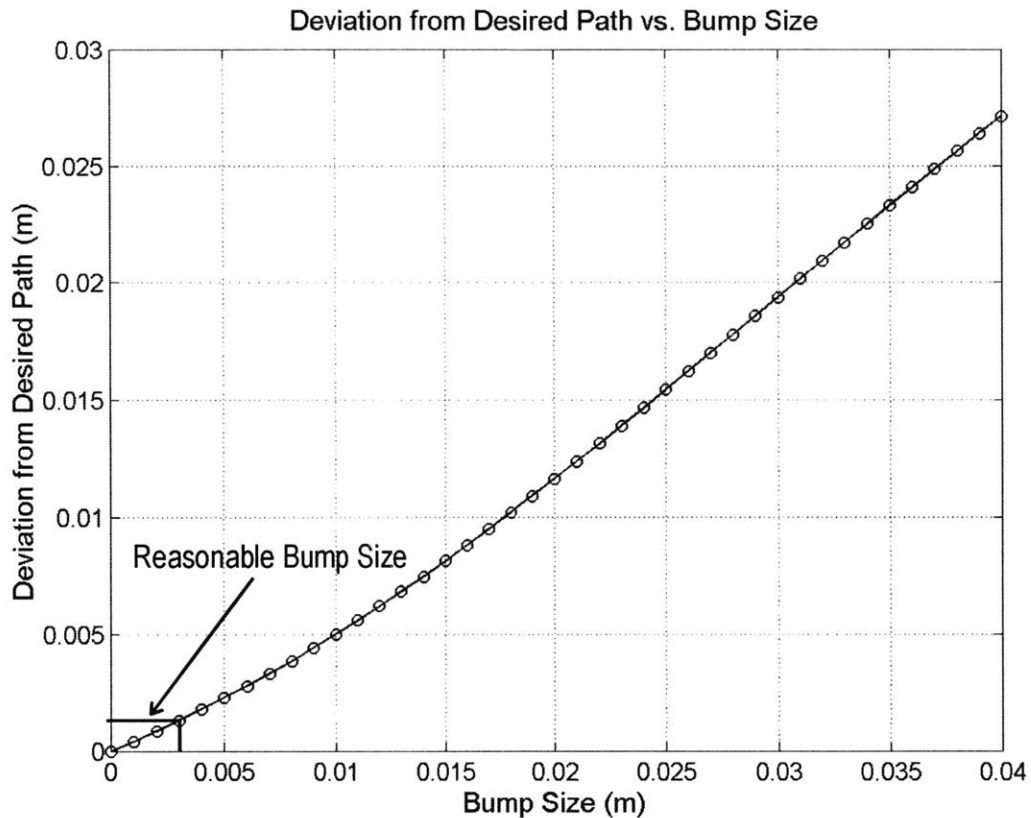
Figure 2-23: Deviation vs. Bump Height

2.5 Conclusions

This chapter addresses the justification of the degree of freedom placed on the SCMM. This chapter has two main points:

- The wheels of the omnidirectional platform with the added joint do indeed touch the ground of an uneven floor.
- The control algorithms designed for a flat floor are valid for an uneven floor

Thus, this chapter justifies design of the suspension joint on the SCMM.

Chapter

3

SmartWalker Stability

This chapter discusses designing the SmartWalker for stability. This includes design tools that ensure the SmartWalker will not slip, tipover, or experience brake failure. Current passive wheeled walkers on the market (see Figure 3-1) have several limitations that were avoided when designing the SmartWalker. Namely, these walkers have instabilities that cause them to either "run away" from the user or tip over.

Figure 3-1: Types of Wheeled Walkers on the Market (Walk Easy)

The standard wheeled walker configuration has two fixed wheels in the rear and two caster wheels in the front. Most often the two rear wheels have brakes that are activated by the user's hands, much like a bicycle brake. Some designs, which are inherently easy to tip over, have only three wheels. Furthermore, all of these types of walkers can run away from people if the user applies a forward force and subsequently does not move his feet. The following sections deal with the prevention of the above described walker instabilities.

3.1 SmartWalker Frame Configuration

The location of the SCMMs and passive casters of the omnidirectional platform is a critical design decision that has a direct impact on the stability of the SmartWalker. Implementing the omnidirectional mobility platform described in Chapter 2 is challenging because the user's stride can easily interfere with the platform. Configurations other than the one presented earlier were considered. Several reasonable configurations of the SmartWalker's frame and SCMM locations are shown in Figure 3-2.
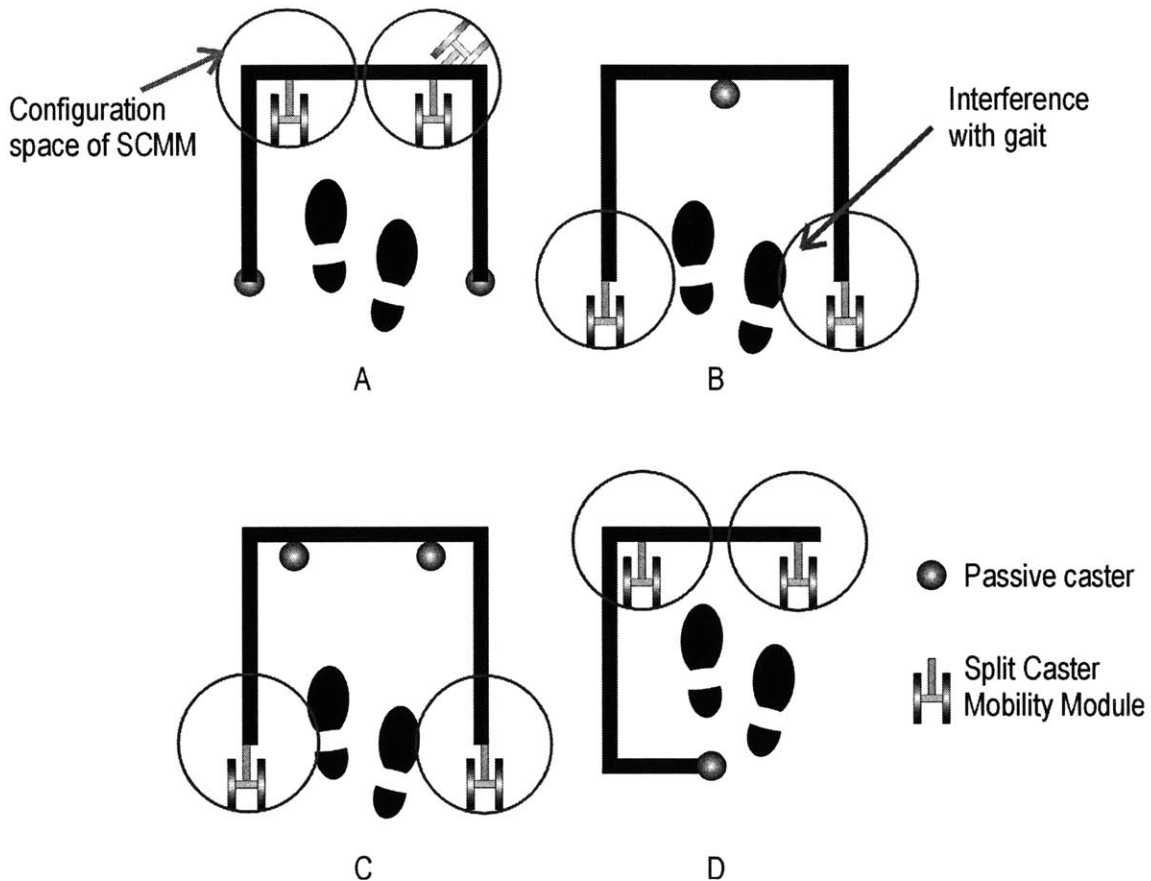
Figure 3-2 Possible Frame Configurations for the SmartWalker

Each SCMM is free to rotate 360 degrees about the encoder shaft, which causes problems when designing the frame. This is shown in Figure 3-2A by displaying the SCMMs in two of their possible positions. The circles that surround the SCMMs represent the total space that the SCMMs can occupy. Care must be taken so that the configuration space of both the SCMMs and passive casters does not interfere with the user's gait. To avoid this, the SmartWalker's frame could have been made so large that

the SCMMs could not come close to hindering the user. However, if the SmartWalker is too large, then it will have problems moving through doors and other tight spaces. Thus, a balance must be made between a walker that is large enough to hold the SCMMs and also small enough to maintain a certain level of maneuverability. This is accomplished by designing the SmartWalker to have the same footprint as a conventional passive walker and a design close to configuration A. A three-wheeled walker (see Figure 3-2B, D) is less stable, and putting the SCMMs in the rear (Figure 3-2B, C) would interfere with the user's stride.

Given the walker wheel configuration, it must be shown that the walker is statically stable. There are three modes of instability in these walkers (Finkel, 1997).

1. The brakes hold, but the wheels slide.
2. The walker tips over.
3. The brakes fail.

3.2 Slipping

In the first case (see Figure 3-3), the user applies a force that results in a normal force on all four wheels and shear force on the braked wheels. Given the coefficient of friction, μ_s, the shear force of wheel i, S_i, and the normal force of wheel i, N_i, if

$$\frac{\sum_{i=1}^{2} S_i}{\sum_{j=1}^{4} N_j} > \mu_s \text{ , then the wheels will slip (Finkel, 1997).}$$
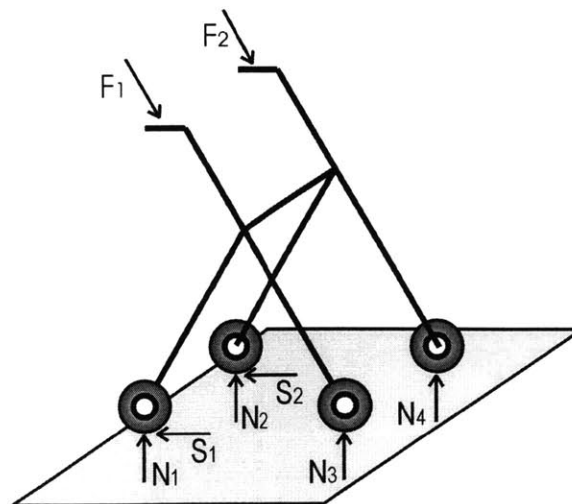
Figure 3-3: Diagram of Four-Wheeled Passive Walker (Adapted from Finkel)

For the SmartWalker, the front two wheels are replaced by the SCMMs, and the rear two wheels are passive casters. The SCMMs are simplified and represented as having a single contact point with the ground. The rear wheels are represented as spherical joints and thus only support normal forces. A free body diagram of the walker is shown in Figure 3-4. A three-dimensional analysis would show that the structure is statically indeterminate since there would be only six equations for eight unknowns, F_{lx}, F_{ly}, F_{rx}, F_{ry}, F_{fx1}, F_{fx2}, F_{by1}, F_{by2}.
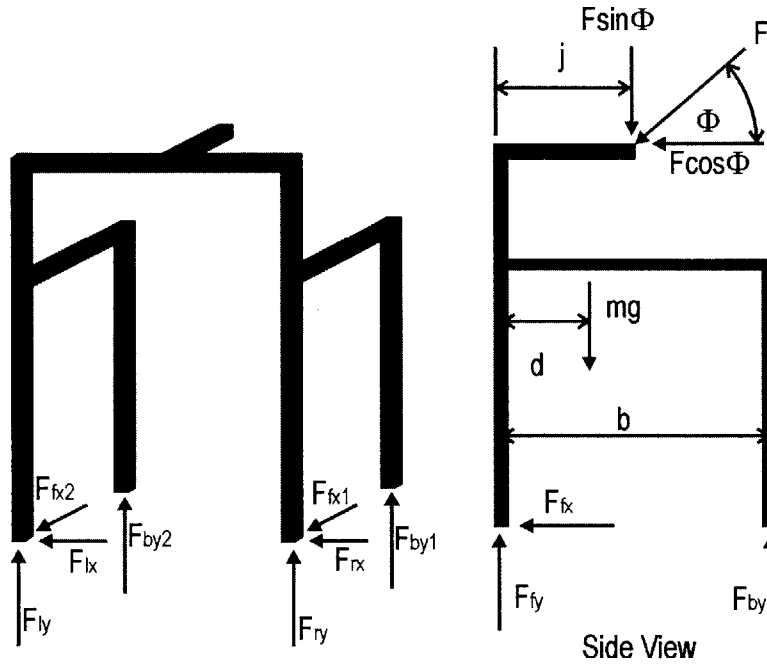
Figure 3-4: Free Body Diagram of 2-D Walker

If it is assumed that the forces acting on the left and right side of the walker are equal, then the forces on the side view of the SmartWalker can be calculated. In this case the following equations apply:

$$\sum F_x = F \cos\phi + F_{fx} = 0 \tag{3-1}$$

$$\sum F_y = -F \sin\theta - mg + F_{fy} + F_{by} = 0 \tag{3-2}$$

$$\sum M_D = 2b(F_{by}) - h(F \cos\phi) - j(F \sin\phi) - d(mg) = 0 \tag{3-3}$$

The sum of the normal forces acting on the legs of the walker is:

$$\sum_{1}^{4} N = F \sin\phi + mg \tag{3-4}$$

40

Figure 3-5 illustrates when the SmartWalker will slip. The different lines represent various masses of the SmartWalker. Any forces above the line will cause slip. As the angle at which the force is applied approaches ninety degrees, the force needed to cause slipping approaches infinity.

Forces That Cause the SmartWalker to Slip
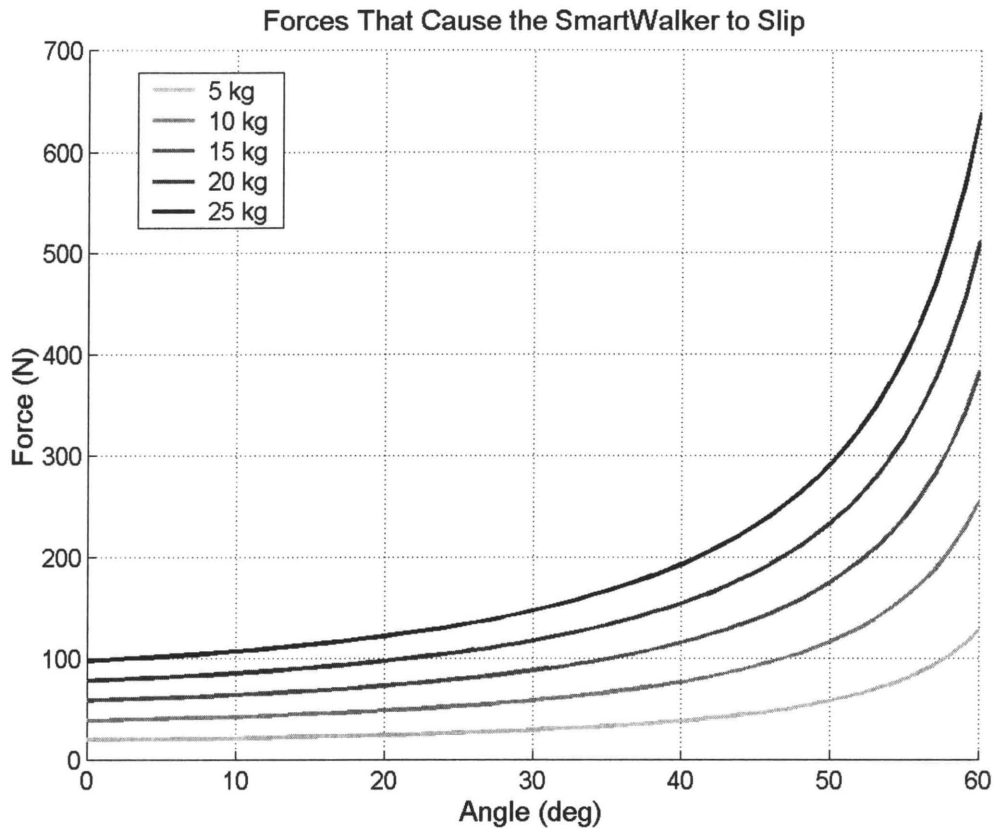
Figure 3-5: Forces That Cause the SmartWalker to Slip (Varying Masses)

This figure shows that although a light walker may be desirable in case it needs to be lifted off the ground, a certain mass does create a more stable walker. It can be assumed that the user would not be applying more than approximately 200 N (Godding, 1999). Even when the user is applying such a large load, it would mostly be in the Z-direction, where Φ is close to ninety. In any case, a mass of approximately 15 kg is a good compromise between stability and lightness. At this weight, only extreme cases of high user applied force coupled with low values of Φ would cause the walker to slip.

3.3 Tip-Over

A simple two-dimensional analysis can show when the walker will tip over, but it is not as accurate as a three-dimensional analysis. Instead, a more detailed stability measure is utilized (Papadopoulos, 1996). It takes into account the walker's mass and height of the center of mass and is applied to the entire walker, not just a 2-D representation of the walker. A brief description of the Papadopoulos stability margin is presented. A more detailed description can be found in Appendix B.

Tipover is described as when "a nominally upright vehicle body undergoes a rotation which results in a reduction of the number of ground contact points such that all remaining points lie on a single line (tipover axis)" (Papadopoulos, 1996). Only the outermost points, those that make up a convex polygon, are considered. This polygon is dubbed a "contact polygon," and is shown in Figure 3-6. Each of the black dots represents a point where a structure touches the ground. Note that one of the black dots lies within the convex polygon and thus does not constitute a vertex of the polygon. There are two different forces, each composed of the weight of the vehicle and any other external forces acting upon the body, that originate from the black and white circle. One of the forces lies within the polygon; the other lies outside of the polygon. The force that lies within the polygon will not cause the structure to tip over, while the other force will.
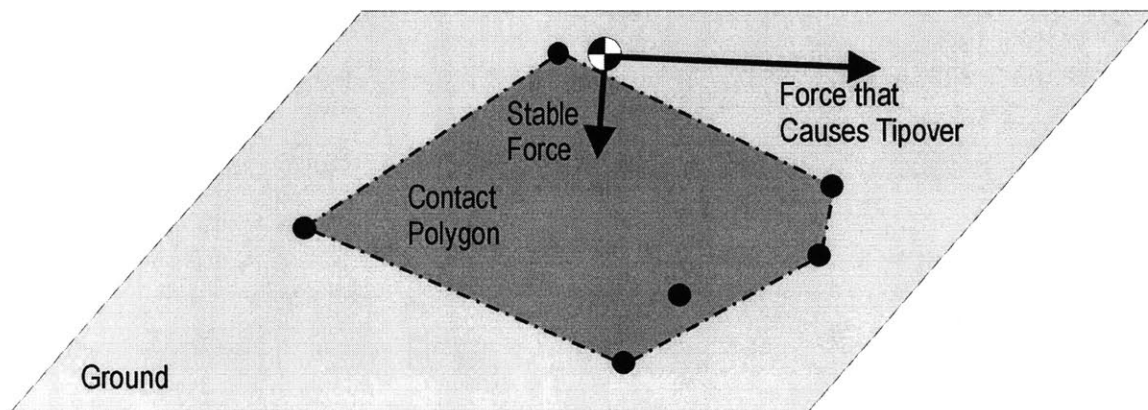
Figure 3-6: Contact Polygon

A scalar stability measure, α, that is a function of the force described above and the angle that the force makes with one of the edges of the contact polygon is described (Papadopoulos, 1996). Specifically,

$$\alpha = \left(\Theta_i\right)_{\min} \|f_r\| \qquad (3\text{-}5)$$

where Θ is the angle between the force vector, $\mathbf{f_r}$, and the vector between the effective center of mass and the line that connects two vertices of the contact polygon. If $\alpha < 0$ then the walker is tipping over. If $\alpha > 0$ then the walker is in a stable state.

The key difficulty in applying this stability analysis to the walker is determining which wheels constitute a convex polygon. This arises because the split caster mobility modules (SCMMs) are constantly changing orientations. Figure 3-7 is a top-down view of the walker that shows the wheels with assigned numeric values.
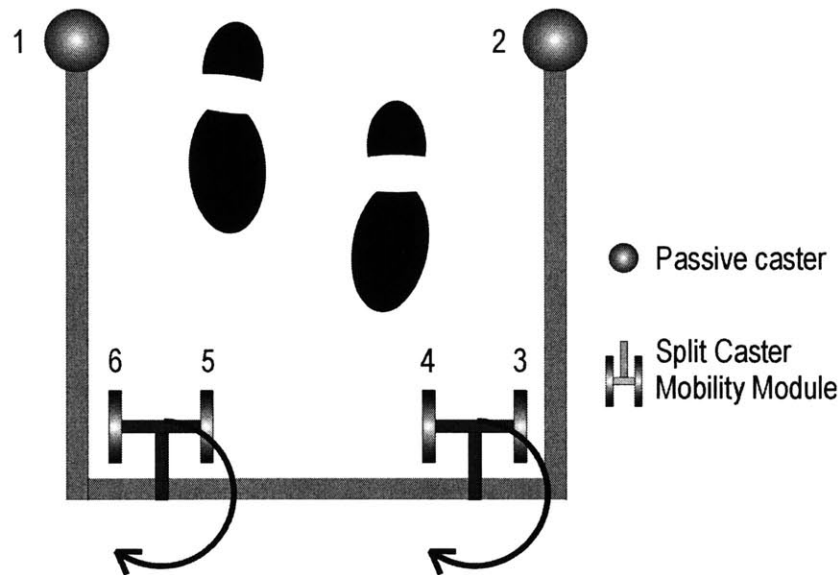
Figure 3-7: Numbering Diagram of the Omnidirectional Platform's wheels

Wheels one and two remain fixed relative to the center of mass of the walker, while wheels three through six rotate as shown by the arrows. The center of mass of the person is assumed to lie either on or in front of the line connecting wheels one and two and thus does not contribute a vertex to the convex polygon. As the SCMMs rotate, different combinations of the wheels will form the convex polygon. This is shown in Figure 3-8. Note the configuration on the left uses wheels one, two, three, and six to form the polygon, while the configuration on the right uses wheels one, two, four, five, and six.

43
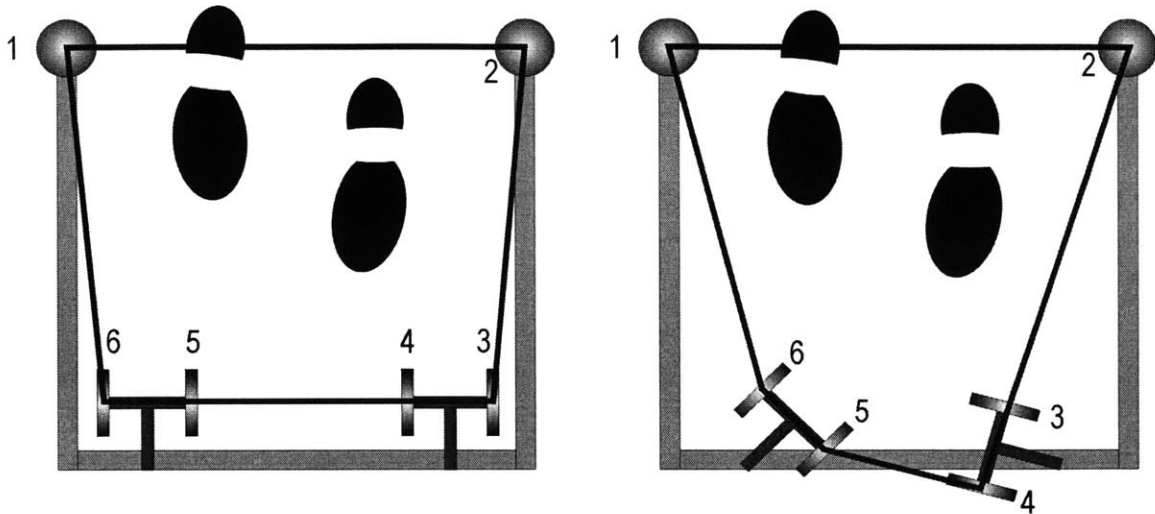
Figure 3-8 (a,b): Two Different Convex Contact Polygons

The algorithm to find which wheels to use works by finding the slopes of the lines from wheel two to wheel one, wheel three to wheel one, wheel four to wheel one, wheel five to wheel one, and wheel six to wheel one. It then finds the maximum value of those slopes. The maximum slope will determine which wheel is the next one to use. This procedure is then repeated for that wheel. After this is completed, the polygon's vertices are set and the procedure for determining the stability margin is given in Appendix B.

This analysis is used as a design tool to make certain that the chosen design is acceptable. Namely, the algorithm answers the question of whether or not the dimensions of the walker will result in a stable system when coupled with reasonable forces. An example of this is shown in Figure 3-9. The diagram shows the position of all six wheels as circles. The location of the encoder shafts are marked with a "+" sign. The center of mass is at the beginning of the "force vector due to mass." The force that is acting upon the force/ torque sensor is $F_x = 10$ N, $F_y = 20$ N, and $F_z = 80$ N. The torque is 1, 2, and 0 Nm for M_x, M_y, and M_z respectively. The dimensions correspond to the SmartWalker's measurements. Note that F_r resides inside the contact polygon, which along with a tipover measure of thirty-one, indicates that the walker is stable and will not tip over.
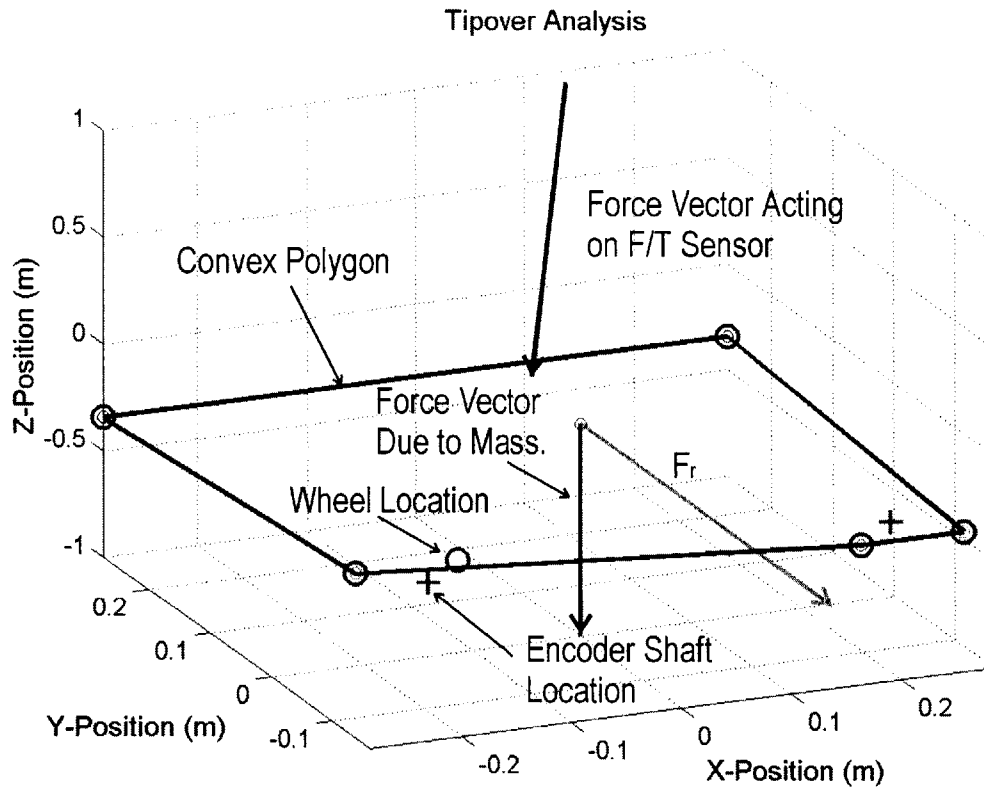
Tipover Analysis

Figure 3-9: Tipover Analysis

3.4 Brake Failure

The SmartWalker does not have any user-applied brakes, but the motors can serve as brakes if they are powered and commanded not to move. Thus, "brake" failure for the SmartWalker will only occur if the torque applied to the motors is greater than the motor stall torque. A free body diagram of the case when all four of the SmartWalker's wheels are facing parallel to the user-applied force is shown below.
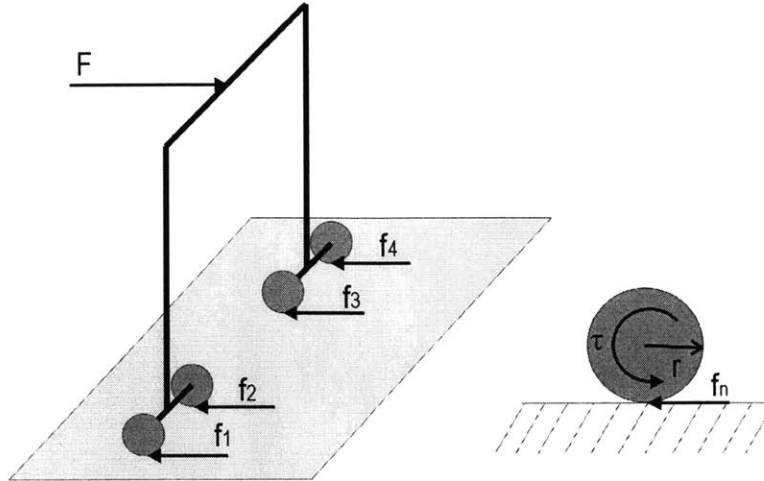
Figure 3-10: Free Body Diagram for Braking

The sum of the forces is:

$$F = \sum_{1}^{4} f_n \qquad (3\text{-}6)$$

where:

$$f_n = \tau \cdot r \qquad (3\text{-}7)$$

and

$$\tau = \tau_{stall} \cdot \rho \qquad (3\text{-}8)$$

where ρ is the gear ratio. The total force that is needed to overcome the motor stall torque is:

$$F = n\left(\frac{\tau}{r}\right) \qquad (3\text{-}9)$$

where n is the number of motors. For the chosen design the result is:

$$F = 4\left(\frac{230 \cdot 28}{39}\right) \qquad (3\text{-}10)$$
$$= 660\,\text{N}$$

This is an exceptional force, and is unlikely to be applied to the SmartWalker.

3.5 Conclusions

The analyses done in this chapter show that the SmartWalker's frame design, footprint, and motor choices are all suitable to prevent the SmartWalker from losing its stability, either through slipping, tipping over, or brake failure.

Chapter

4

Mechanical Design

The focus of this chapter is the detailed mechanical design of the SmartWalker. The chapter includes the justifications of the design decisions regarding the wheels, the housing that holds the motors, gears, and wheels together, the slip rings, the bearings, the axles, the encoder shaft, the motors, and the frame. A photograph of the final product is shown below. It shows the SCMMs, the camera for the vision system, the acoustic sensors, and the computer housing.
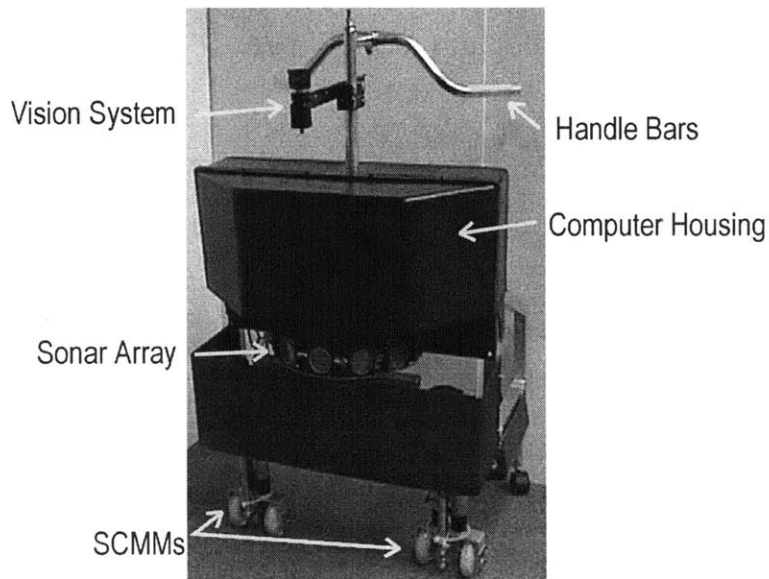
Figure 4-1: Photograph of the SmartWalker

4.1 Wheel Design

There are numerous types of wheels available on the market that could be used in the SmartWalker. Inline skating wheels are used because they have a uniform hub size and come in various profiles and material hardness. This allows the wheels to be changed easily without modifying the design. Figure 4-2 shows the makeup of an inline skate wheel with different available profiles.
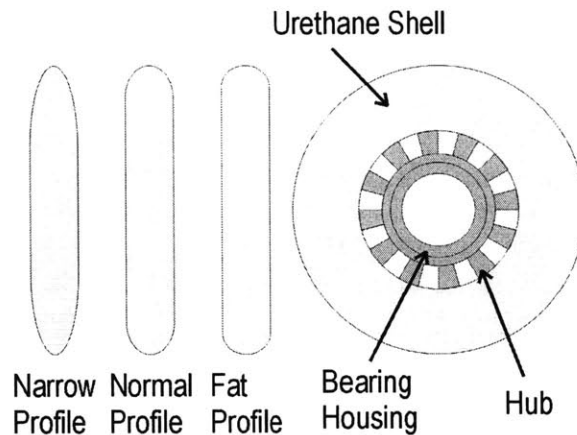
Figure 4-2: Wheel Profiles and Composition (Adapted from Bachman, 1997)

There has been some research on the properties of inline skate wheels and their application to mobile robots. The following conclusions have been made (Bachman, 1997):

1. Increasing the load increases the wheel compression, friction force, and contact patch size;

2. Increasing the diameter increases the friction force and contact patch size;

3. Increasing the durometer (hardness) decreases the wheel compression, friction force, and contact patch size;

4. Increasing the radius of the profile increases the friction force and contact patch size, but decreases the compression;

5. Increasing the durometer and the radius of the profile in combination decreases the compression;

6. Increasing the diameter and the radius of the profile in combination increases the friction force;

7. Increasing the load and the radius of the profile in combination increases the friction force;

8. Increasing the diameter and the durometer in combination increases the area of the contact patch.

A large diameter wheel is necessary for the SmartWalker since it needs to overcome small obstacles and bumps in the floor. With that in mind it is desirable to find a wheel that has a small friction force. Without doing extensive experiments, it can be surmised from the above statements that the best type of wheel for the SmartWalker would be one with a narrow profile.

4.2 Housing Design

The housing, or the part that connects the wheels, gears, motors, and slip rings, needs to be small, lightweight, and be made out of one piece (see Figure 4-3). It needs to be small because as shown in Figure 3-2, a large housing might create interference with the user's stride. It needs to be lightweight since it is a major component of the walker. It needs to be made from one piece of material since the two independent wheel axles need to lie on the same line.
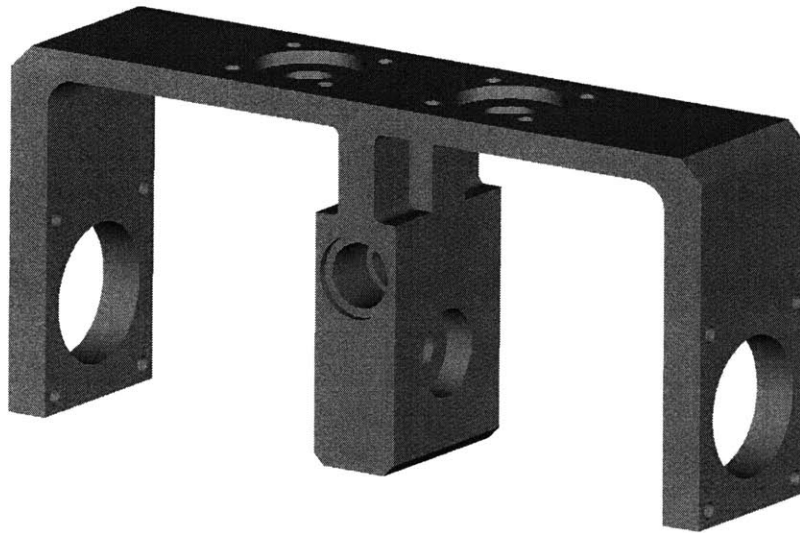
Figure 4-3: SCMM Housing

Figure 4-4 shows the four different gearing systems that were considered. The first is a worm gear drive. The second is a belt gear drive similar to the system used on the omnidirectional test platform (Yu, 2000). The third and fourth are both bevel gear

designs. The former has the motors positioned above the wheels, while the latter has the motors positioned on the same horizontal plane as the wheels. Of the four possible designs, the vertical bevel gear is used for the housing. Its vertical design limits the possibility of interference with the user's gait and is overall less space consuming than the other designs.
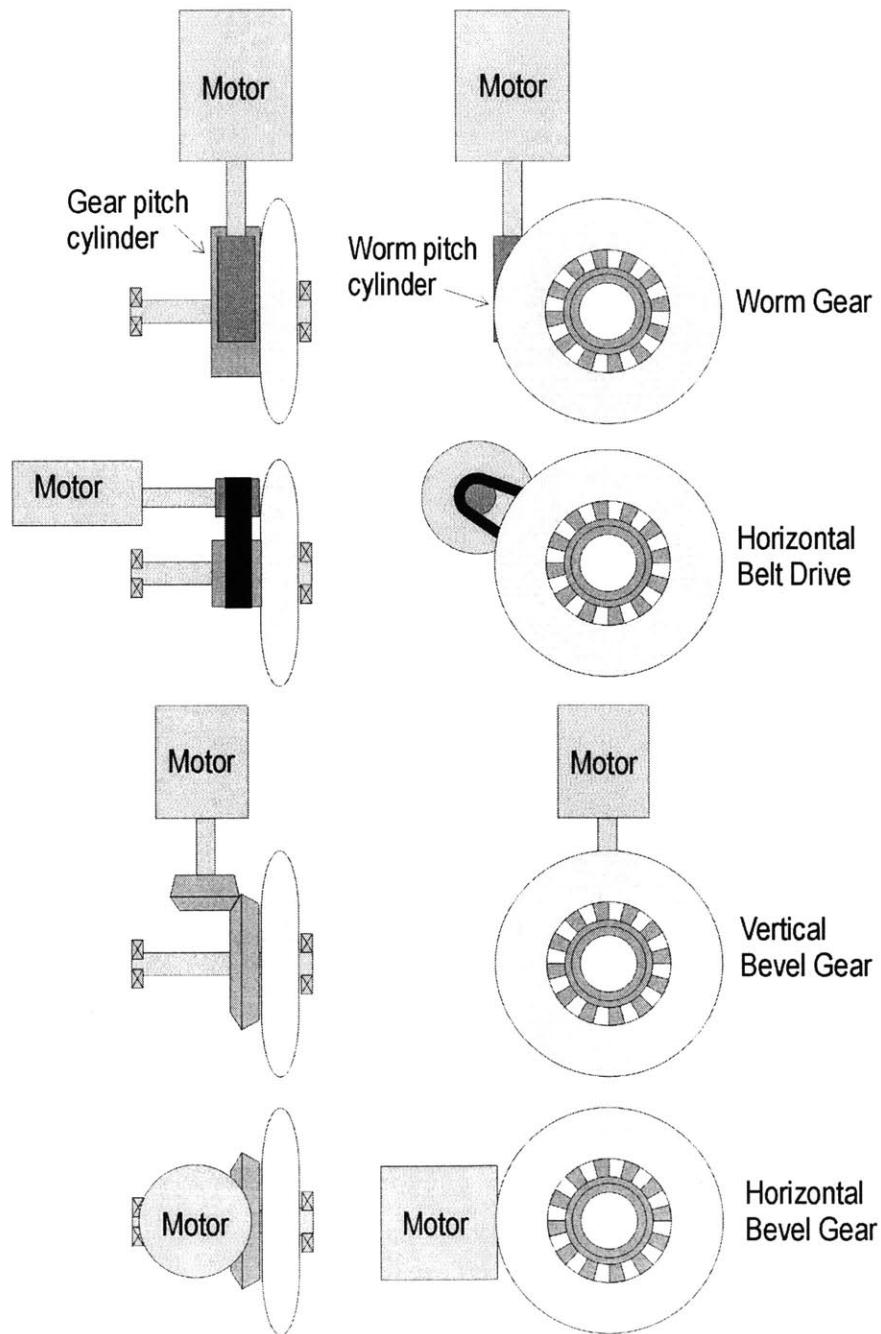
Figure 4-4: Worm and Drive Belt Gearing Systems

4.3 Slip Ring Design

Because the SCMMs need to rotate more than 360 degrees, the wires that are connected to the motors can become wrapped around the encoder shaft. There are six wires that need to be connected to each motor: positive and negative power lines for the motors and +5 V, ground, and two signal channels for the motor encoders. It must be noted that the motors and the motor encoders cannot share a common ground because the motor's polarity is switched when running backwards. One of the simplest methods to prevent the wires from wrapping around the encoder shaft is a series of slip rings. Slip rings are conductive rings that maintain electrical conduction through a mechanical contact between two rotating parts.

The placement of the slip rings in the electrical circuit is the main design concern. It is beneficial to keep the slip rings as small as possible to reduce complexity in the design. Thus, it is desired to find the place in the electrical circuit where the least number of wires needs to be severed.

A diagram of the electrical circuit is shown in Figure 4-5. It shows three possible locations to place the slip rings. Location A would require the motor controllers and motor amplifiers to lie on the SCMM. If that were the case, the computer would need twenty lines of data to be sent to the SCMM. Those twenty lines coupled with four power lines would require twenty-four slip rings. Location B would keep the motor controllers near the computer, but place the motor amplifiers on the SCMM, requiring twelve slip rings. Location C places nothing on the SCMM except the motors and their encoders, resulting in ten slip rings. Thus, C minimizes the number slip rings and is the logical choice.

51
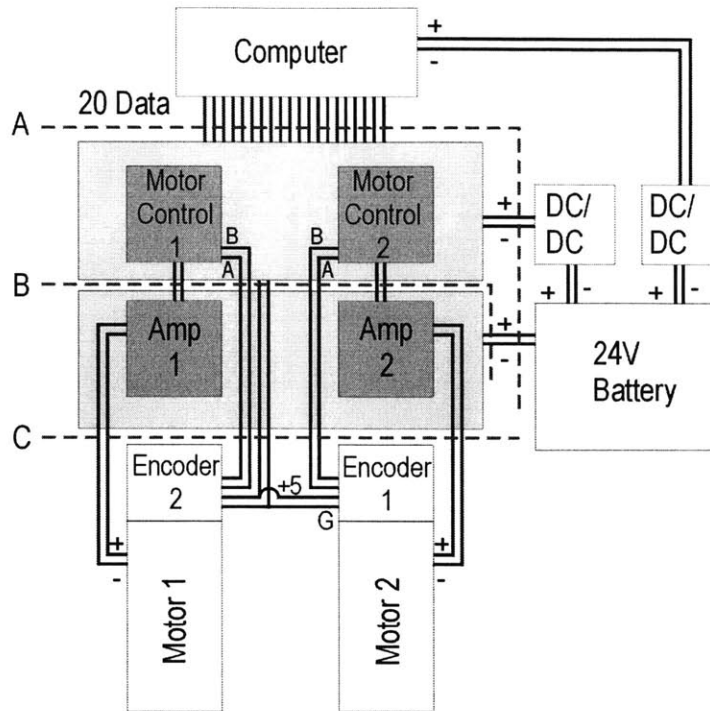
Figure 4-5: Electrical Diagram and Possible Places to Put Slip Rings

Most slip rings on the market are built for high speeds and long wear life; these can cost anywhere from $1000 and up. Some on the market sell for as little as $300 but are bulky and heavy. The walker's requirements are low speeds, lightweight, and a wear life that is significantly shorter than those found on the market. As a result, the slip rings for the SCMM were designed and built at MIT. A diagram of the slip ring design is shown in Figure 4-6.
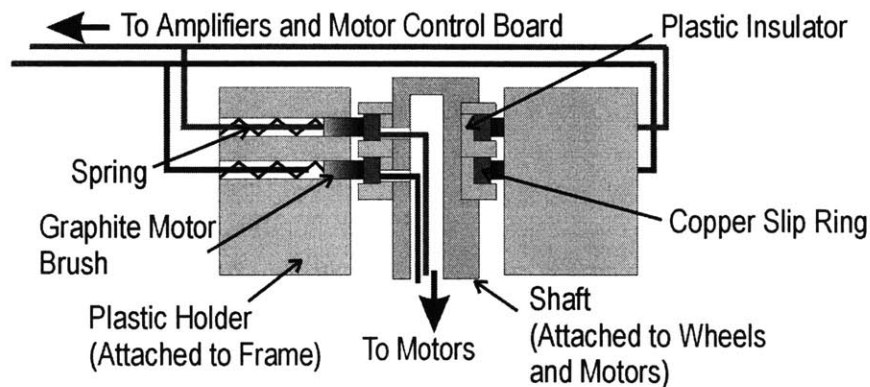
Figure 4-6: Slip Ring Diagram

A drawing of the completed slip ring is shown below.
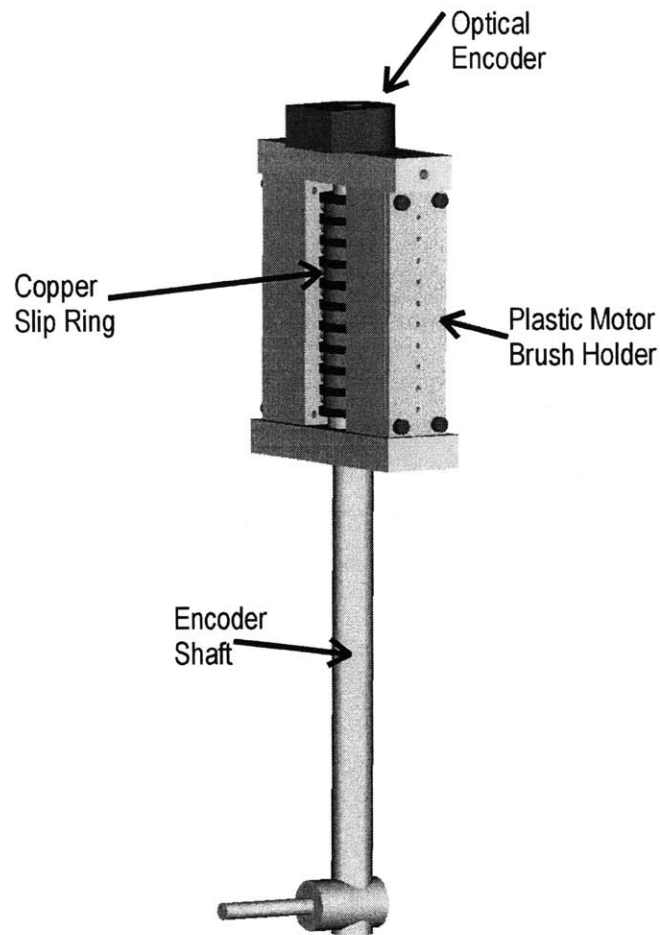
Figure 4-7: Slip Rings

The slip rings are designed to be vertical, narrow, and lightweight. The springs guarantee that the brushes will maintain contact with the copper rings as the shaft rotates. The second brush for each ring is a redundant feature. If the first brush loses contact, then the second brush will maintain the electrical connection.

The resistance in each of the slip rings was tested at various angular positions of the encoder shaft. Figure 4-8 shows this relationship for the ten slip rings of one of the SCMMs.
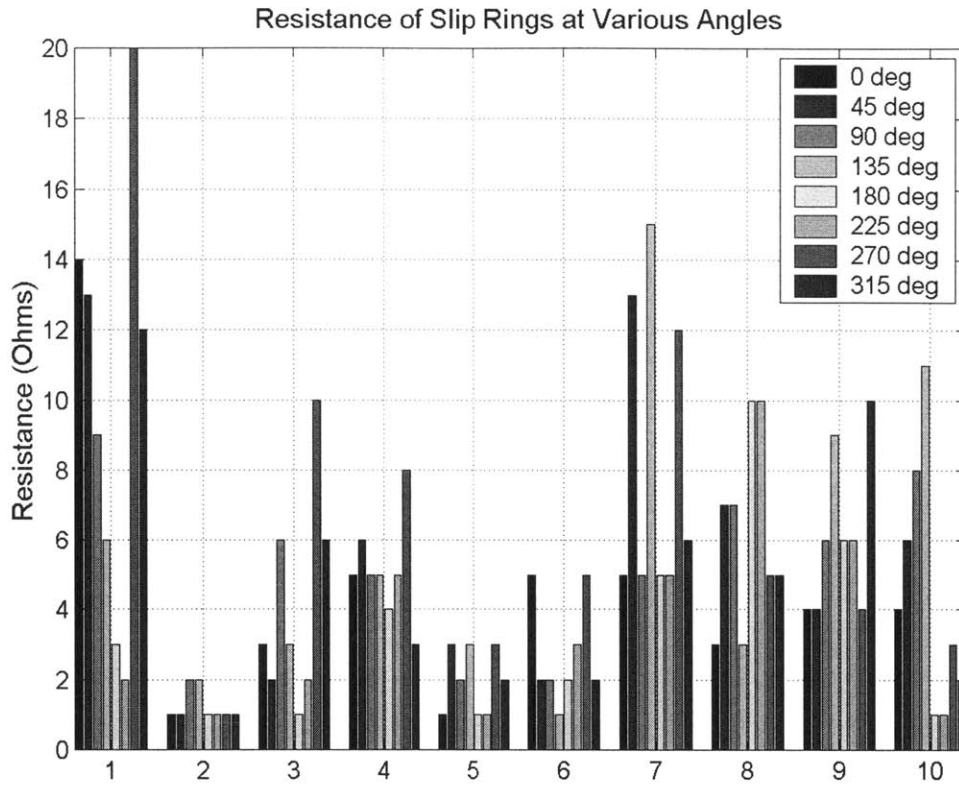
Figure 4-8: Resistance of Slip Rings at Various Angles

Note that the resistance in the slip rings changes dramatically depending on its position. Also note that there are significant differences between different channels of the slip rings. Furthermore, although not shown in the figure, there is a spike in the resistance as the shaft is rotated. These changes in resistance and the large spikes are caused by three different defects in the slip rings, which are shown in Figure 4-9.
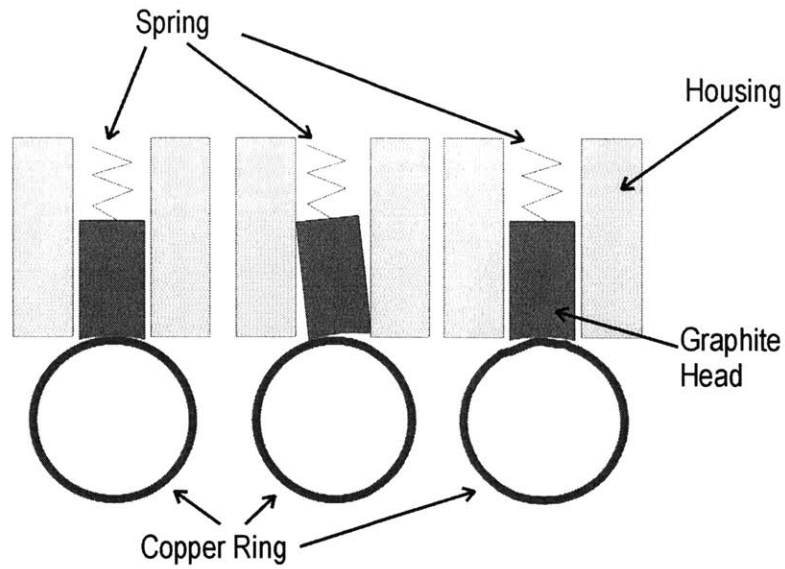
Figure 4-9: Problems That Some of the Slip Rings Have

The left part of the figure shows how the graphite head's radius does not always match that of the copper ring. The middle part of the figure demonstrates how extra room in the housing allows the graphite head to slide back and forth as the shaft is rotating. This is most likely the cause of the spike in resistance mentioned earlier. The right side of the figure illustrates the irregularity of the copper ring. This lowers the contact area between the graphite head and the copper ring. All of these problems could be solved with better manufacturing processes; nonetheless, the slip rings perform up to specifications.

4.4 Bearing and Axle Design
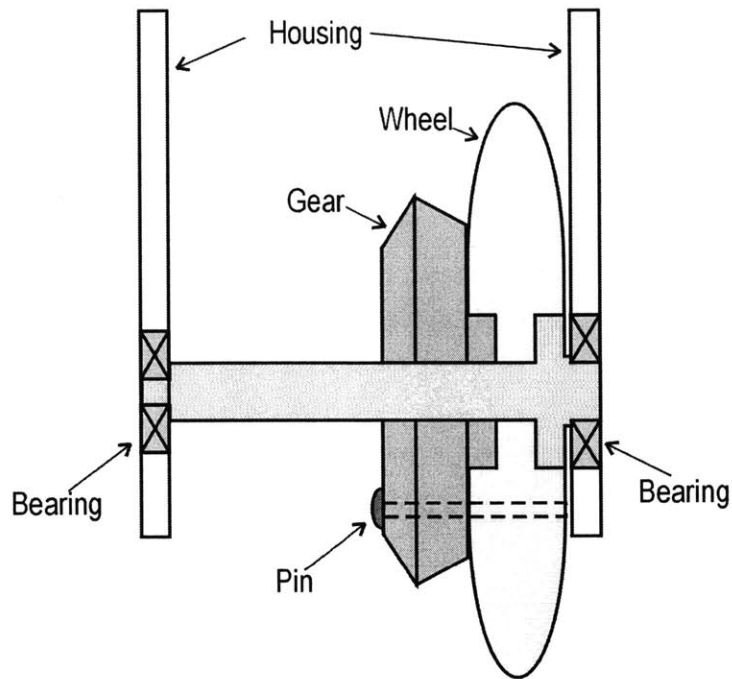
Figure 4-10: Wheel, Gear, and Axle Diagram

The axle, wheel, and gear diagram is shown in Figure 4-10. The pin is a screw that prevents slipping between the gear and wheel. A drawing of the axle, wheel, and gear is shown below. The gear teeth are replaced with a pitch angle for simplification.
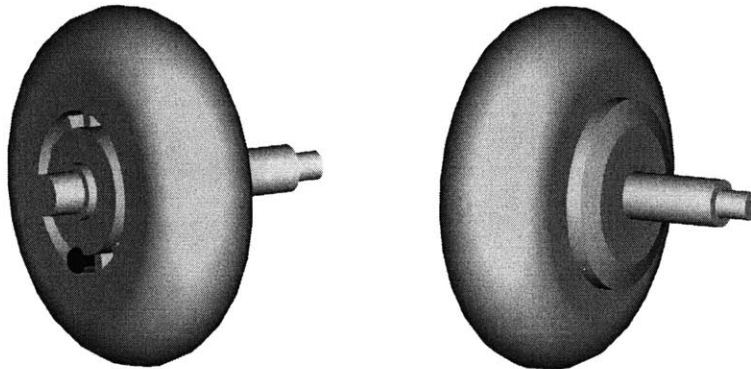
Figure 4-11: Wheel, Gear, and Axle

4.4.1 Bearing Design

To determine the proper bearing sizes, an assumption is made that the forces act on the midpoint of the gears. Although the actual forces act at a point between the

midpoint and the large side of the gear, this assumption gives minimal error. The following is based on work done by (Shigley, 1989).
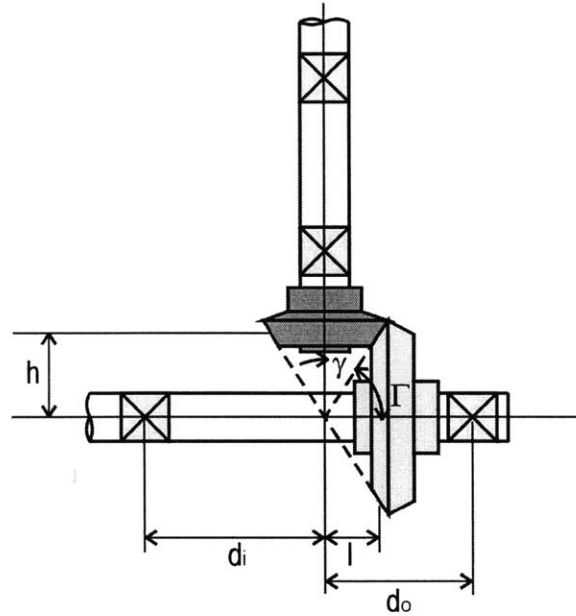
Figure 4-12: Diagram of Bevel Gears (Adapted from Shigley, 1989)

The force that acts on the gear tooth, **W**, can be broken down into three components, W_t = tangential, W_r = radial, and W_a = axial. These components are shown in Figure 4-13.
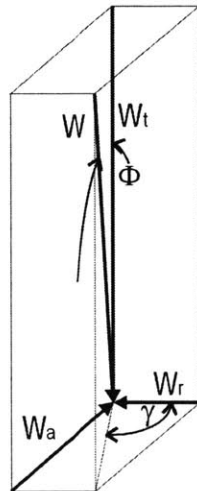
Figure 4-13: Components of Force Acting on Gear Tooth (Shigley, 1989)

The known values are the pressure angle, α; pitch angle, Γ; motor torque, T_m; radius of gear at its midpoint, r; distance to inner bearing, d_i; distance to outer beating, d_o; distance to wheel, l; distance from axle to pinion, h; and reaction force, **F_r**.
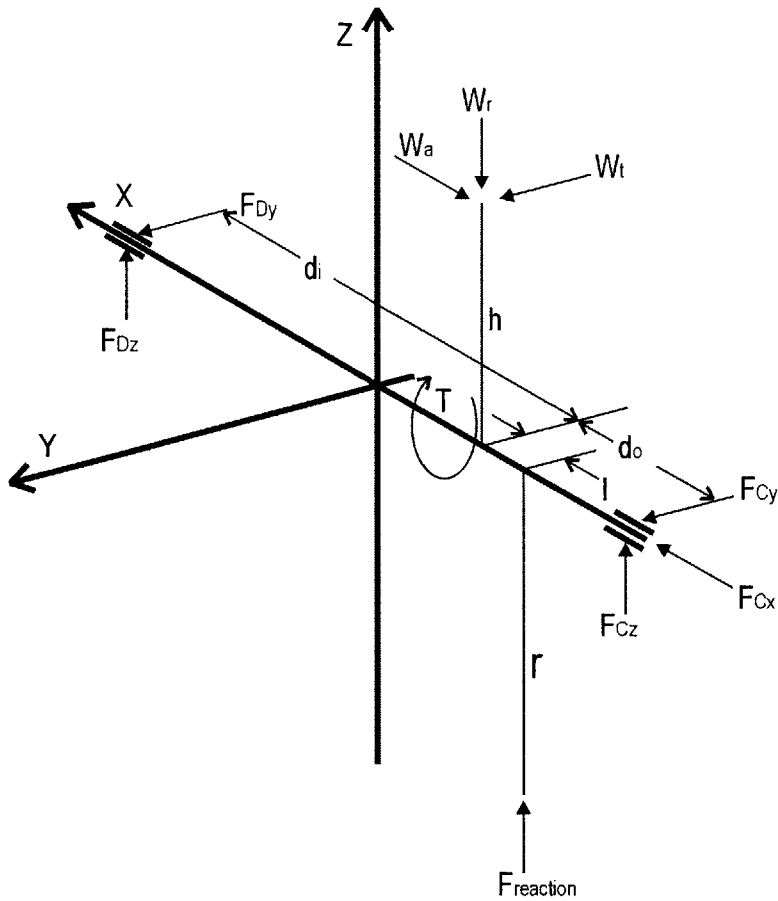
Figure 4-14: Bevel Gear and Bearing Free Body Diagram

To determine the forces acting on the bearings, the moments about bearing D are summed. The position vector from D to G is:

$$\mathbf{R}_G = -d_i \mathbf{i} + h\mathbf{k} \tag{4-1}$$

The position vector from bearing D to bearing C is:

$$\mathbf{R}_C = -\left(d_i + d_o\right)\mathbf{i} \tag{4-2}$$

The position vector from bearing D to the reaction force from the wheel/ground contact point is:

$$\mathbf{R}_R = -\left(d_i + l\right)\mathbf{i} - r\mathbf{k} \tag{4-3}$$

Summing the moments about D:

$$\mathbf{R}_G \times \mathbf{W} + \mathbf{R}_C \times \mathbf{F}_c + \mathbf{R}_R \times \mathbf{F}_{\text{reaction}} + \mathbf{T} = 0 \qquad (4\text{-}4)$$

yields:

$$\begin{vmatrix} \mathbf{i} & \mathbf{j} & \mathbf{k} \\ -d_i & 0 & h \\ -W_a & W_t & -W_r \end{vmatrix} + \begin{vmatrix} \mathbf{i} & \mathbf{j} & \mathbf{k} \\ -(d_i+d_o) & 0 & 0 \\ F_C^x & F_C^y & F_C^z \end{vmatrix} + \begin{vmatrix} \mathbf{i} & \mathbf{j} & \mathbf{k} \\ -(d_i+l) & 0 & -r \\ 0 & 0 & F_{reaction} \end{vmatrix} + T\mathbf{i} = 0 \quad (4\text{-}5)$$

Thus,

$$T = h * W_t \qquad (4\text{-}6)$$

$$F_C^z = \frac{d_i(W_r) + h(W_a) - (d_i + l)F_{reaction}}{(d_i + d_o)} \qquad (4\text{-}7)$$

$$F_C^y = -\frac{(d_i)W_t}{(d_i + d_o)} \qquad (4\text{-}8)$$

using

$$\mathbf{F}_D + \mathbf{F}_C + \mathbf{W} + \mathbf{F}_{\text{reaction}} = 0 \qquad (4\text{-}9)$$

$$F_C = W_a\mathbf{i} - \frac{(d_i)W_t}{(d_i + d_o)}\mathbf{j} + \frac{d_i(W_r) + h(W_a) - (d_i + l)F_{reaction}}{(d_i + d_o)}\mathbf{k} \qquad (4\text{-}10)$$

$$F_D = -\frac{(d_o)W_t}{(d_i + d_o)}\mathbf{j} + \frac{d_o(W_r) - h(W_a) + (d_i + l)F_{reaction}}{(d_i + d_o)}\mathbf{k} \qquad (4\text{-}11)$$

For the chosen design the result is:

$$\mathbf{F}_C = -9.48\mathbf{i} - 6.40\mathbf{j} - 47.18\mathbf{k} \qquad (4\text{-}12)$$

where T_m is the stall torque and is equal to 206 mNm, r_{av} equals 7.5 mm, W_t equals the stall torque divided by r_{av}, Φ is 20 degrees, Γ is 71.56 degrees, W_r equals $W_t * \tan(\Phi) * \cos(\Gamma)$, and W_a equals $W_t * \tan(\Phi) * \sin(\Gamma)$.

using $F_{reaction} = 70$ N yields:

$$\mathbf{F}_D = 0\mathbf{i} - 6.40\mathbf{j} + 50.34\mathbf{k} \qquad (4\text{-}13)$$

The bearing chosen for position C has a load rating of 495 N and the one chosen for position D has a load rating of 3,350 N. As one can see, both bearings are more than suited for the application.

4.4.2 Axle Design

The material for the axle needs to be resistant to corrosion. Two materials were considered: aluminum and stainless steel. It needs to be determined if the weight savings that aluminum offers over steel are worth the reduction in strength. The volume of the axle is 6.986 cm^3. That corresponds to a weight of 50.9 g for stainless steel and approximately 19.5 g for the aluminum, a savings of 31.4 g. There are four axles on the SmartWalker, so the weight savings of using aluminum over stainless steel are only 125.6 g. Since the weight savings are minimal, stainless steel was chosen as the axle material.

4.5 Shaft Analysis

There should be little to no deflection in the encoder shaft of the SCMM. Most of the dimensions of the SCMM's encoder shaft are determined by other factors such as the motor size and wire diameters. Nonetheless, the shaft's weight should be kept to a minimum. This begs the question of whether to build the shaft out of stainless steel or aluminum. Thus, calculations must be made to determine how much deflection will occur. These calculations are based on work done by (Shigley, 1989).

If the shaft were to be perfectly loaded along its axis, then there would be a load, $P_{critical}$, that would cause the shaft to buckle. However, no shaft is perfectly loaded along its axis. Given e, the eccentricity of the applied load or the distance between the load and the shaft axis, it can be shown that e can be replaced with a load P along the axis and a moment $M_A = P*e$ as shown in Figure 4-15.
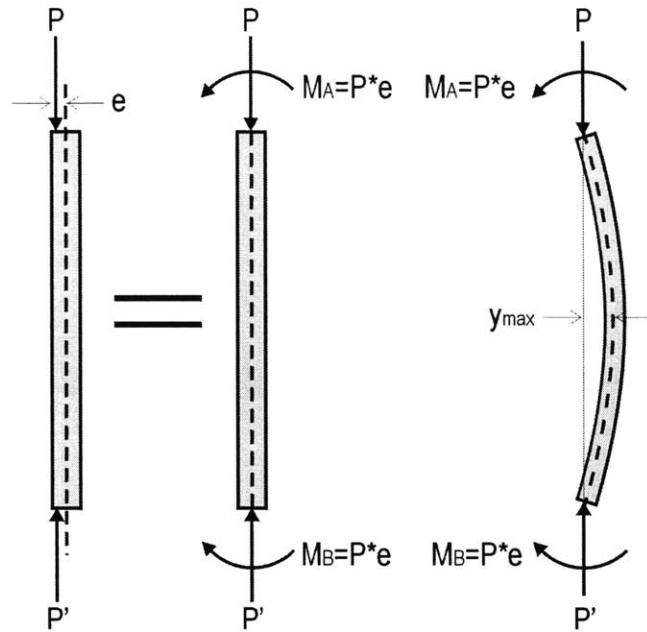
Figure 4-15: Eccentric Load, its Equivalent, and a Shaft Being Bent by an Eccentric Load (Shigley, 1989)

The maximum deflection is given as:

$$y_{max} = e\left[\sec\left(\sqrt{\frac{P}{EI}}\frac{L}{2}\right) - 1\right] \qquad (4\text{-}14)$$

where y_{max} is the amount of deflection at center of shaft (see Figure 4-15), e is the eccentricity of load, P is the load, L is the length of shaft, E is the Modulus of Elasticity, and I is the moment of inertia.

The majority of the shaft has a large groove running through it. This groove is necessary to hold the wires that pass through the slip ring to the motors and motor encoders. A drawing of the slip ring shaft is shown in Figure 4-16a, and a representation of the cross sectional area of the shaft is shown in Figure 4-16b.

Figure 4-16 (a,b): Encoder Shaft and Cross-Sectional Area of Encoder Shaft

The encoder shaft must have a diameter wide enough to retain a certain amount of material in the thinnest areas. For this reason, a shaft diameter of 15 mm is used. In addition, values of 8 mm for h and 9.5 mm for w are used.

Since this groove is along the majority of the shaft, its moment of inertia is used. An estimate of its moment of inertia is given as:

$$I_x = \frac{1}{4}\pi r^4 - \left(\frac{1}{12}wh^3 + whd^2\right)$$

where r is the shaft radius and d is the distance from the center of the shaft to the midpoint of the rectangle.

Plugging in the values of 7.5 mm for r and 2.75 mm for d yields $I_x \approx 1.5e^{-9}$ m^4. Using 300 mm for L and 100 N for P $y_{max} \approx e(.011)$ for aluminum and $y_{max} \approx e(.004)$ for stainless steel.

Thus, the stainless steel shaft will bend approximately two to three times less than the aluminum shaft. Furthermore, using aluminum only offers a weight savings of 0.24 kg, which is nominal. Thus stainless steel is used as the material for the encoder shaft.

4.6 Determining the Proper Motors

Although the walker needs to travel at a maximum of 0.4 m/s, the wheels on the SCMMs need to move faster as shown in Figure 4-17. The graph is the result of a simulation that determines the wheel speeds given a desired walker speed. In this case, the desired walker speed is 0.4 m/s and the SCMM's initial position is normal to the

desired direction of travel. As one can see, the second wheel needs to travel at a speed of over 0.6 m/s in order for the walker to achieve its desired velocity.
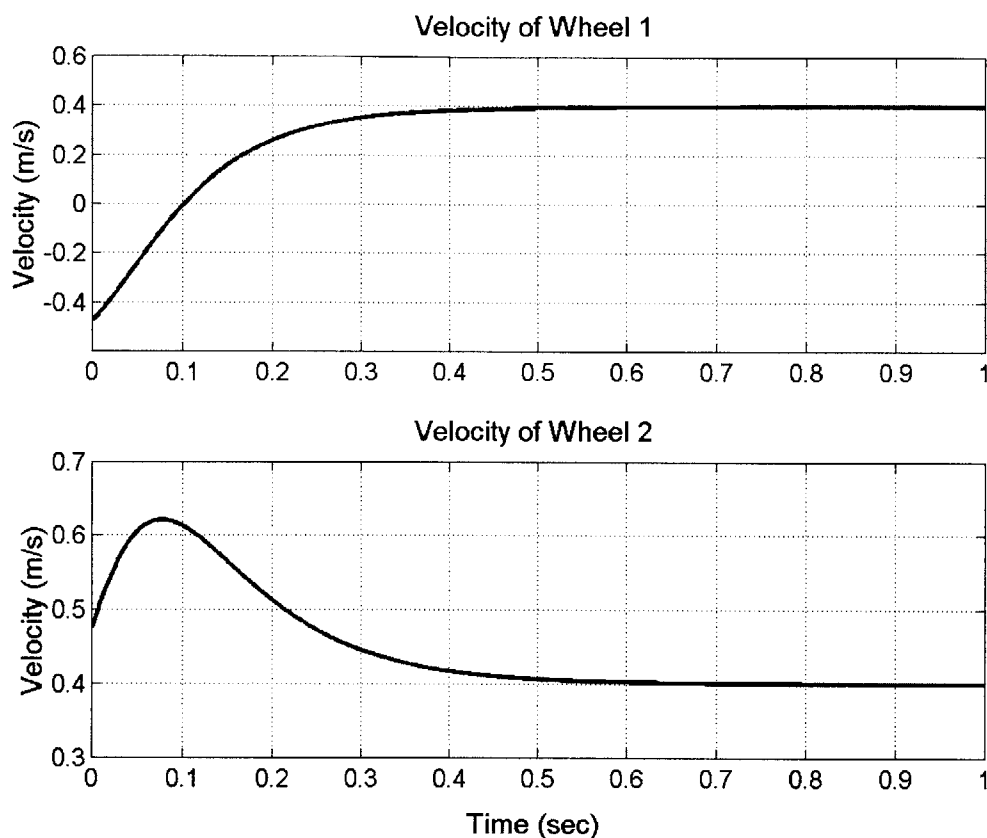
Figure 4-17: Wheel Speed (Adapted from Yu)

The requirements of the motor are that it be lightweight, powerful enough to drive the walker while the user is applying his body weight, inexpensive, able to be driven by the motor amplifiers that the SmartWalker uses, and have a small diameter. The motor amplifiers that are used, LMD180201, have a peak output of 6 A and a continuous output of 3 A. Thus, the motors need a startup current less than the peak output of the amplifiers, and a continuous current level less than the continuous output of the amplifiers.

The motors that are used are 20 W Maxon A-max motors, part number 110851. The motor's characteristics are outlined in the chart below.

Table 4-1: Motor Specifications

Characteristic	Value	Units
Assigned power rating	20	W
Nominal voltage	24	V
No load speed	6440	rpm
Stall torque	206	mNm
Speed/torque gradient	31.7	rpm/mNm
No load current	64.6	mA
Starting current	5860	mA
Terminal resistance	4.09	Ω
Max. permissible speed	6000	rpm
Max. continuous current	1350	mA
Max. continuous torque	47.3	mNm
Max. power output at nominal voltage	34200	mW
Max. efficiency	80.0	%
Torque constant	35.1	mNm/A
Speed constant	272	rpm/V
Mechanical time constant	14.3	ms
Rotor Inertia	43.0	gcm^2

The motor is coupled with planetary gear head (Maxon part number 110365). Its specifications are charted below.

Table 4-2: Gear Specifications

Characteristic	Value	Unit
Gear ratio	14:1	-
Max. continuous torque	2.25	Nm
Max. intermittent torque	3.38	Nm
Weight	162	g
Max. permissible radial load 12 mm from flange	140	N
Max. permissible axial load	120	N
Mass inertia	1.687-1.87	gcm^2
Recommended input speed	<5000	rpm

In addition, each motor is coupled with an HEDS-5540 three-channel encoder, part number 110513. This encoder has a resolution of 500 counts/turn.

Several calculations are used to determine if this motor is acceptable. First, the gear ratios and wheel diameters need to be set. The diameters of the wheels used are 76 mm. This is an approximate number although other diameter wheels could be used if desired. Wheel diameters range from 60 to 100 mm, and the most common diameters

range between 72 and 78 mm. The gear ratio of the bevel gears is 2:1, giving the total ratio of 28:1 (fourteen from the planetary gear head and two from the bevel gears).

The following equations are taken from (Maxon, 1999). The velocity of the wheels, using the no-load maximum speed of the motors is given by:

$$V_{wheel} = \left(\frac{V_{motor_{max}}}{\rho} \right) 2\pi r \qquad (4\text{-}15)$$

where $V_{motormax}$ is the maximum speed of motor, ρ is the gear ratio, and r is the radius of wheel.

Plugging in the appropriate numbers yields $V_{wheel} = 0.92$ m/s which is well above the required speed. If the motor is only run below the recommended speed of the gear heads, 5000 rpm, then $V_{wheel} = 0.71$ m/s. It must be noted that these numbers are calculated using the no-load speed of the motors, which are not an accurate representation since there is a load present on the motors. A graph of the motor speed versus the wheel speed is shown in Figure 4-18.
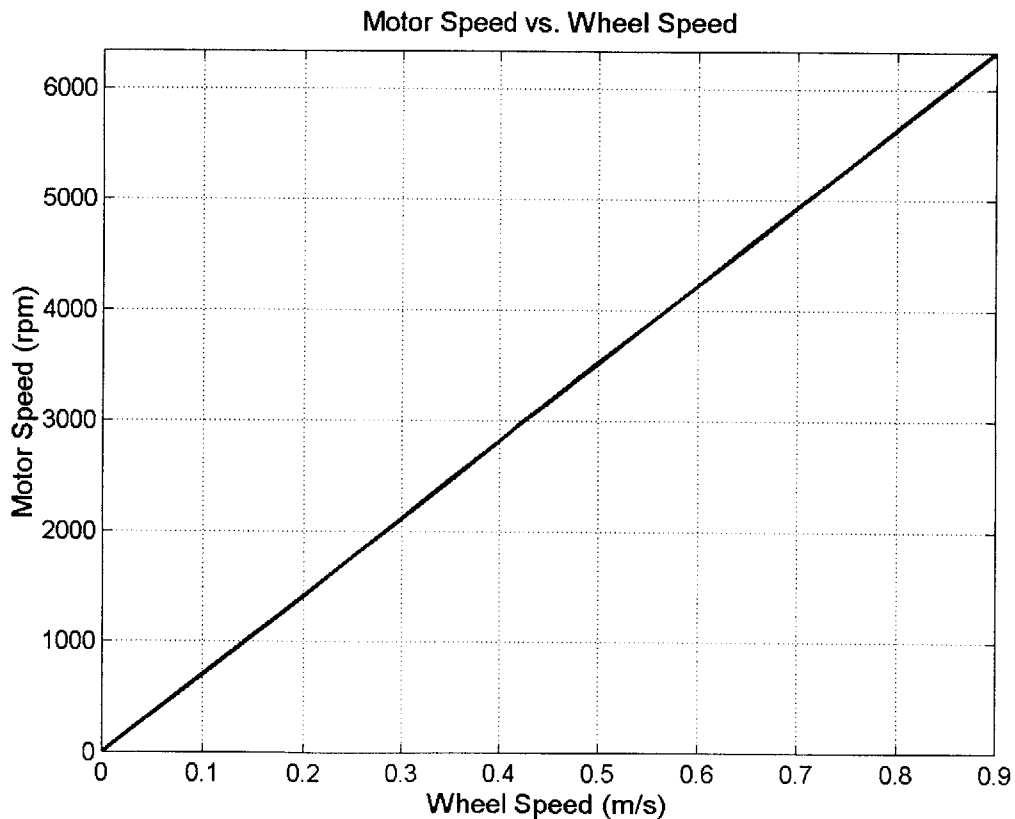
Figure 4-18: Motor Speed vs. Wheel Speed

To determine the maximum velocity that the wheels can generate under a load, the following equation is used:

$$\rho\left(\frac{V_{wheel}}{2\pi r}\right) = V_{motor} = \frac{30}{\pi}\omega_i\left(1 - \frac{M + M_R}{M_{iH}}\right) \tag{4-16}$$

where M is the torque output, M_R is the friction torque, M_{iH} is the generated stall torque, and ω_i is the ideal angular speed.

Rearranging Equation (4-16) and solving for the torque output yields:

$$M = \left(M_{iH}\left(1 - \rho\frac{V_{wheel}}{60r\omega_i}\right)\right) - M_R \tag{4-17}$$

This equation is used to plot Figure 4-19, which shows the motor torque versus the wheel speed, the current versus the motor torque, and the 20 W limit of the motor. The maximum allowable torque, which is above the 20 W limit, is the most torque that the motors can generate; however, it is not recommended that the motors operate above that limit for extended periods of time.
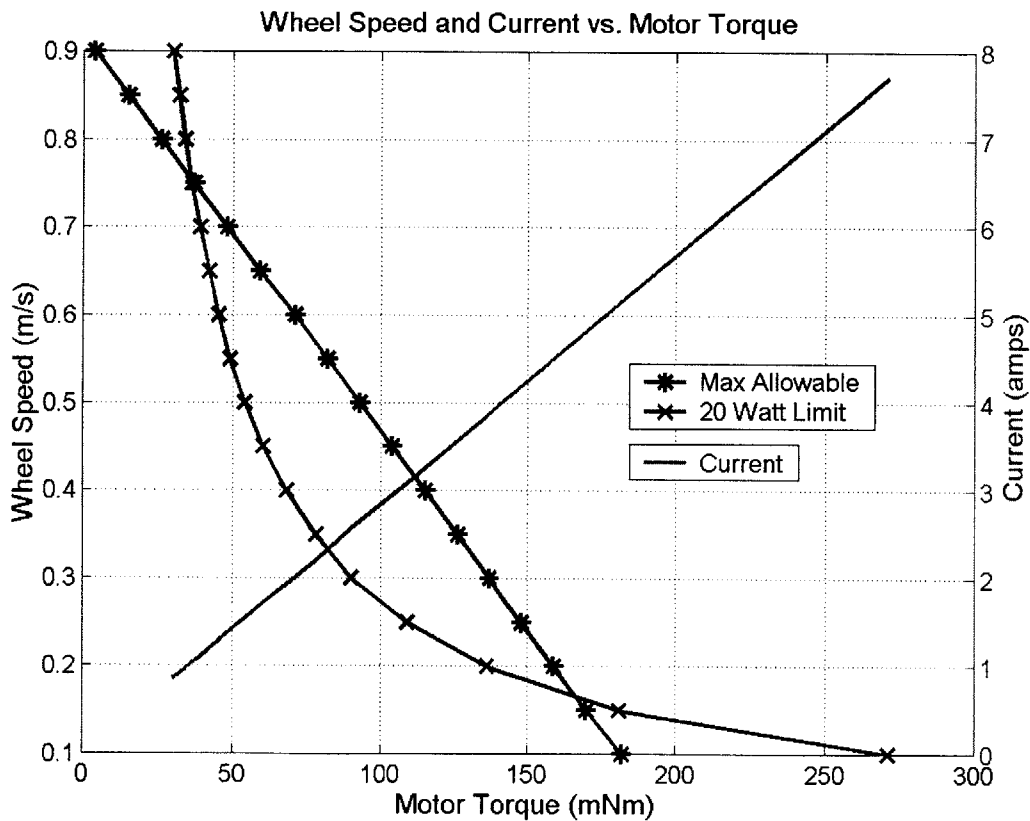
Figure 4-19: Walker Speed and Current vs. Motor Torque (Adapted from Maxon, 1999)

Figure 4-19 shows that the walker should be able to run at the appropriate speed even under the most severe loading conditions. Most likely, when a user is traveling at high speeds, he is feeling confident and not relying on the walker for support. On the other hand, if the user is leaning heavily on the walker, then most likely he is travelling at slow speeds.

To determine how much load is on the motor, it is assumed that each one of the wheels experiences an equal fraction of the load that the user applies to the walker. The amount of torque needed from the motors to keep the wheels rolling is given as:

$$P * r \equiv W * b \qquad (4\text{-}18)$$

where W is the force acting on the wheel (N), P is the force required to keep the wheel rolling (N), μN is the friction force that retards the forward motion of the wheel (N), b is the coefficient of rolling friction (m), and r is the radius of wheel (m) (see Figure 4-20) (Beer, 1998).
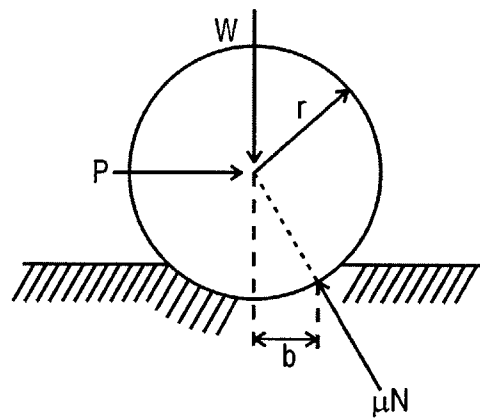
Figure 4-20 Rolling Friction (Adapted from Beer, 1998)

The value of b is difficult to determine both theoretically and experimentally, but it is a value smaller than the amount the wheel is compressed against the floor. For the wheels that were used, a good approximation is 8 mm. An approximation of the user's maximum applied load is 150 N, although most user's would probably apply a load of under 100 N. Using the higher load, the motors would need to output a torque of 200 mNm. Referring back to Figure 4-19, it can be seen that this value approaches the limits of the motors, but nonetheless is within the motor's capabilities. Thus, the chosen motors are deemed suitable for the application.

4.7 Frame Design

The frame is designed to be lightweight and to hold the SCMMs, sonar array, computer and electronics, batteries, and the force/ torque sensor. The frame without any of its components attached is shown in Figure 4-21.
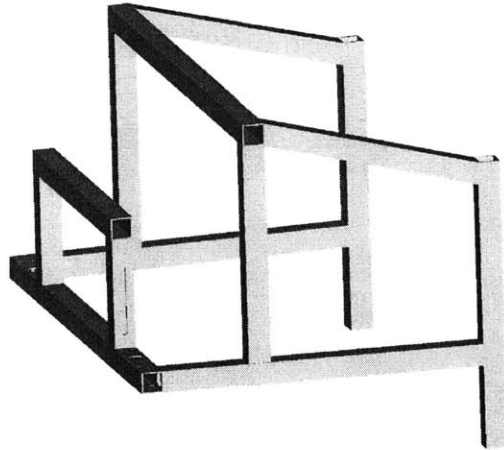
Figure 4-21: SmartWalker Frame

The frame needs to be a certain size in order to hold the slip rings and allow the encoder shaft to pass through (see Figure 4-22).
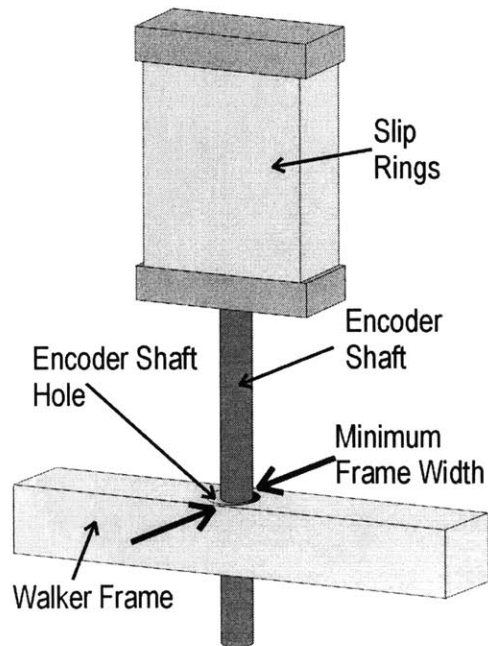
Figure 4-22: Slip Ring Being Inserted into Frame

With that in mind, the minimum acceptable frame thickness is found to be approximately 25 mm. Possible materials for the frame include steel, aluminum, and Star Linear extruded aluminum. An example of a Star Linear beam is shown in Figure 4-23.
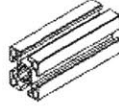
Figure 4-23: Star Linear Extruded Aluminum (Rexroth Star)

In order to decide which material is the most suitable, the best combination of weight and deflection needs to be determined. The beam that connects to the force/torque sensor is one of the parts of the frame that experiences the most deflection. The amount of beam deflection is given to be:

$$y_{max} = \frac{PL^3}{48EI}$$

(4-19)

where P is the load on the beam, L is the length of the beam, E is the modulus of elasticity, and I is the moment of inertia (Beer, 1988).

The moment of inertia for a hollow square beam is given by:

$$I = \frac{1}{12}\left[(bh^3) - (b - 2t)(h - 2t)^3\right]$$

(4-20)

where h, t, and b are shown in Figure 4-24.
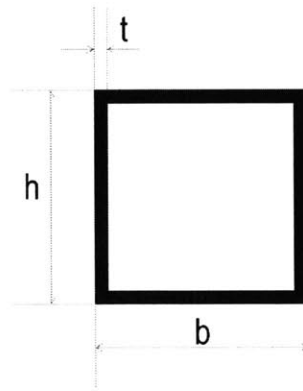
Figure 4-24: Diagram of Frame Cutaway

A comparison of the different materials is shown below.

Table 4-3: Frame Material Properties

	Star Linear	Steel A	Steel B	Aluminum
Size	25x25 (mm)	1" x 1"	1" x 1"	1" x 1"
Wall Thickness	N/A	0.035"	.049"	0.062"
Weight	5.0 kg	2.75 kg	3.9 kg	1.7 kg
Moment of Inertia (cm^4)	1.3 x-dir 2.0 y-dir	0.87	1.17	1.42
Deflection with 100 N Load	0.39 mm : x-dir 0.24 mm : y-dir	0.21 mm	0.1 mm	0.34 mm

As one can see, the aluminum bends more than one-and-a-half times the 0.035" thick steel and more than three times the 0.049" thick steel. However, the actual deflection is extremely small. Therefore, the aluminum is a better choice for material because of its weight savings of approximately 2.2 kg over the thicker steel bar. The weight savings is not as pronounced when compared to the thinner steel tubing; however, a certain thickness is beneficial for attaching items such as the fairings to the frame.

4.8 Conclusions

The SmartWalker's mechanical design focused on the SCMMs, the slip rings, and the frame. Care was taken to keep the SmartWalker lightweight without compromising strength in critical areas. Overall the design is robust and meets the design specifications given in Chapter 1.

Chapter

5

SmartWalker Experimental Evaluation

The experiments done on the SmartWalker focus on four things: the power consumption, the motor time response, the walker time response, and the path following accuracy of the system when used as an autonomous vehicle. This chapter describes and shows the results of the experiments.

5.1 Power Requirements

There are three main power draws of the system: the computer, the electronics, and the motors. Figure 5-1 shows the current as the computer boots. At the end of the startup process the computer uses approximately 3.0 A with all of the PC104 cards connected. This occurred when the central processing unit was running at idle. However, when the SmartWalker is being used, the computer's processor will be running at full speed. Thus, an experiment was run to determine the power requirements under those conditions. The results of that experiment are shown in Figure 5-2. As one can see the theoretical (6.77 A) and the actual (6.7 A) values are very close.
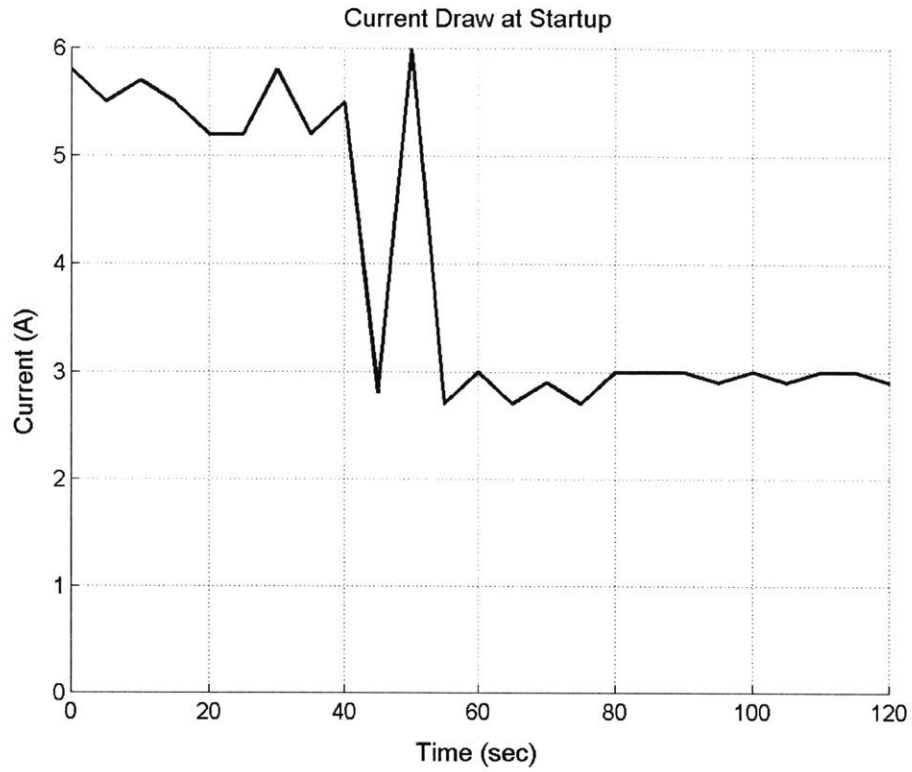
Figure 5-1: Current Used by Computer at Startup
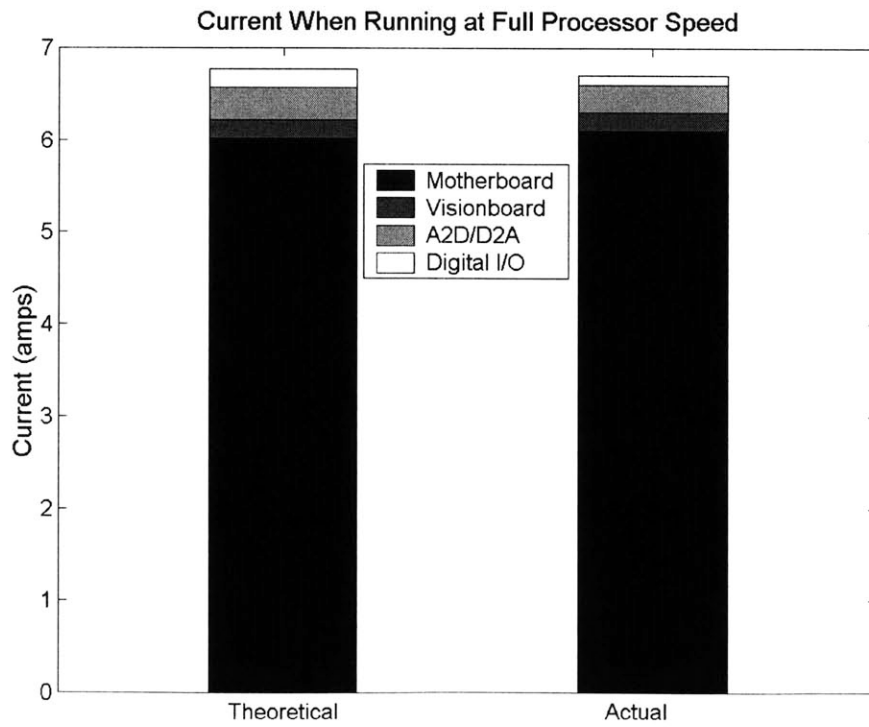
Figure 5-2: Theoretical vs. Actual Current Use at Full Processor Speed

The experiments show that when running at full speed, the computer consumes approximately 35 W. If the four motors are running at their maximum of 20 W then the entire walker uses approximately 115 W when running. The batteries are rated at 120 Wh, which means that the walker can run for approximately one hour if running at full speed. This would allow an elderly person to move approximately 1500 m before the SmartWalker needs to be recharged. Although the total distance that an elderly person moves in a day is not known, it can be assumed that it would consist of moving short distances with long intervals of rest. During these rest periods, the SmartWalker could enter a power conservation mode. Thus, the SmartWalker should be able to be used for an entire day before needing to be recharged.

5.2 Motor Response

The motor controllers generate a trapezoidal speed profile as shown in Figure 5-3. This is to guarantee that the motors do not receive too excessive of a jolt. The acceleration of the motors can be tuned, which causes the acceleration slope to increase or decrease.
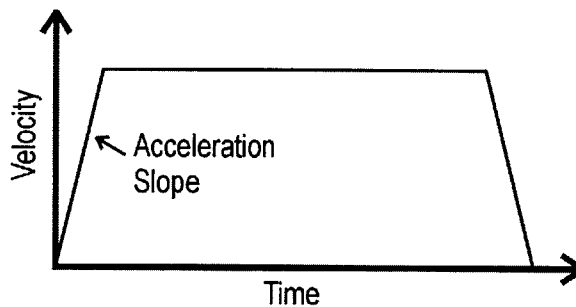
Figure 5-3: Velocity Profile of Motors

A plot of the normalized motor response of all four motors is shown below. The thick line represents the commanded velocity to the motors. Note that the velocity of the motors is discrete. This is because the motor velocity is read as encoder counts. The computer counts the encoder ticks of the motor encoders, which in turn is converted into a velocity.
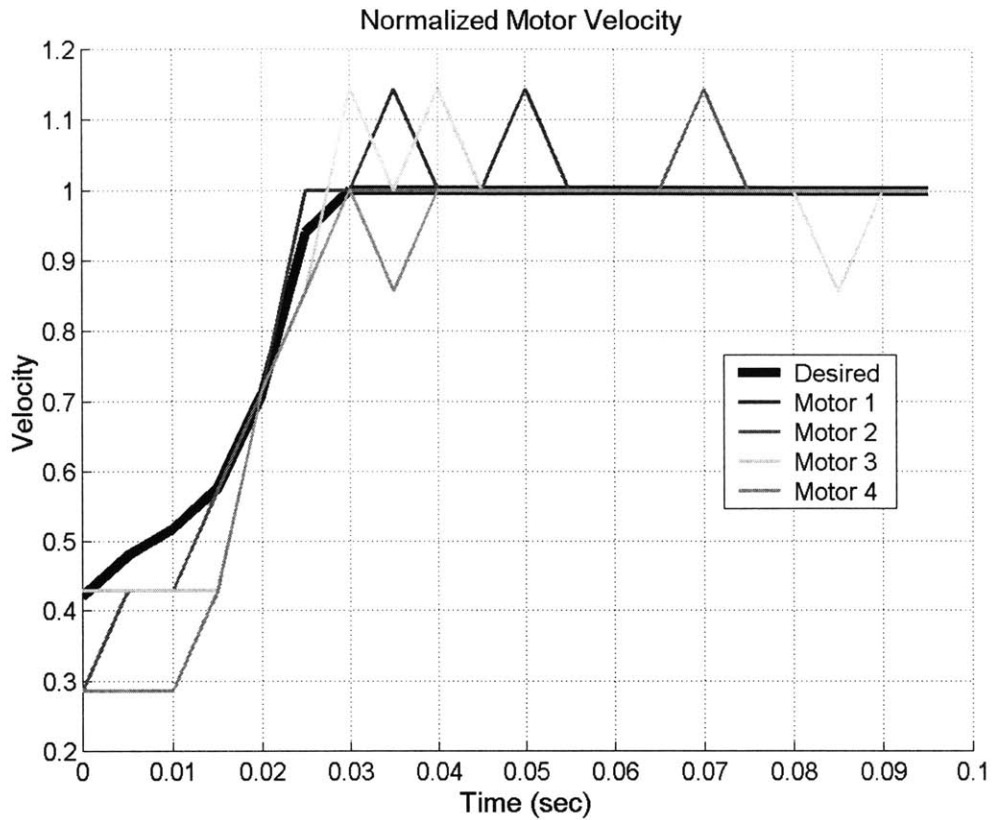
Figure 5-4: Normalized Motor Response

5.3 SmartWalker Time Response

The SmartWalker was outfitted with an incremental encoder that could record the distance that the SmartWalker travels in a straight line. The setup is shown in Figure 5-5.
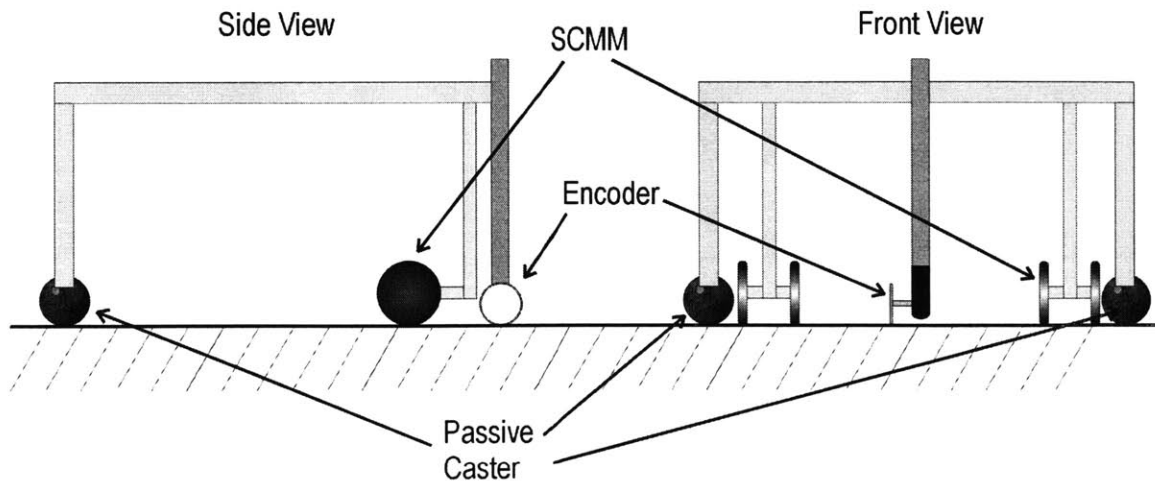
Figure 5-5: Experimental Setup

Because the encoder is in a fixed position, the SmartWalker can only move forward and backwards when the encoder is touching the ground. For this test, the walker is commanded to move in a straight line starting from zero velocity. The distance the SmartWalker travels is recorded and differentiated twice to yield velocity and acceleration profiles. The results for a commanded speed of 0.1 m/s are shown in Figure 5-6. The three different lines represent the results of three trials.
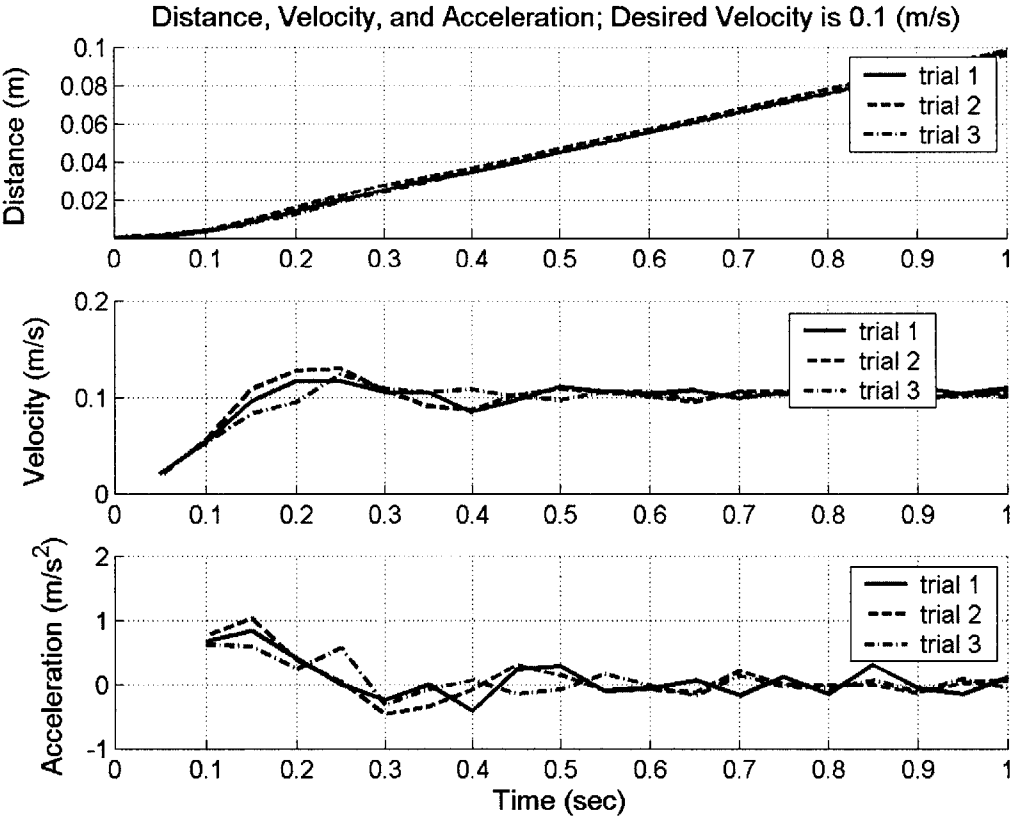
Figure 5-6: Distance, Velocity, and Acceleration vs. Time

Note that the velocity profile is close to the step response of the system. Figure 5-7 shows this in greater detail along with an approximation of the system, assumed to be second order. The approximation of the system, which appears as the thick line, was found using a natural frequency of $\omega_n \approx 15$ (rad/sec) and a damping ratio of $\varsigma \approx 0.4$.

Therefore, the transfer function of the system is $\dfrac{225}{s^2 + 12s + 225}$. The three dashed lines represent three different trials.
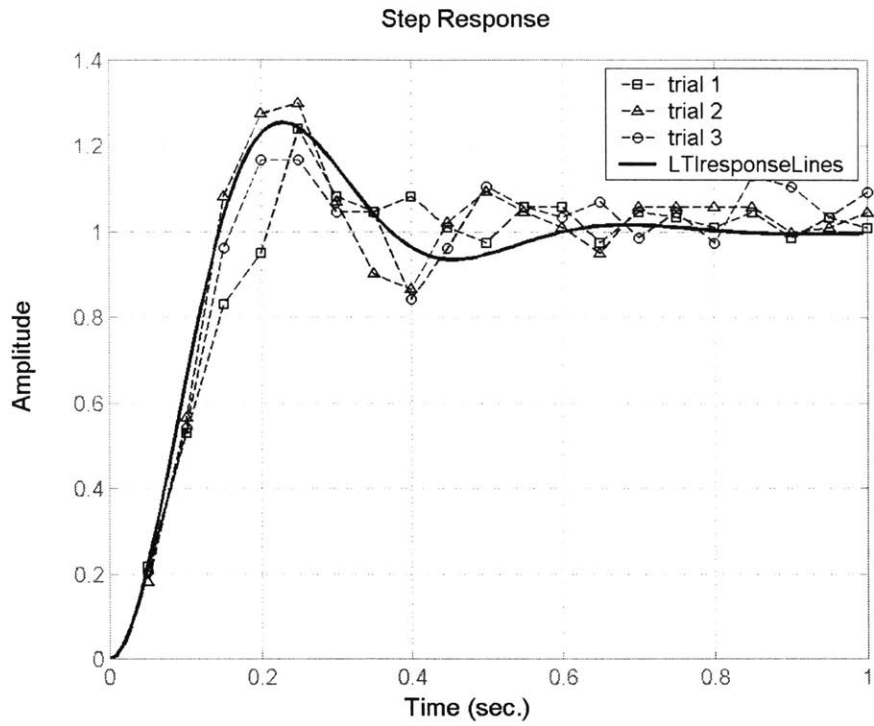
Step Response

Figure 5-7: Approximate Step Response of System

A bode plot of the approximation of the system is shown in Figure 5-8.
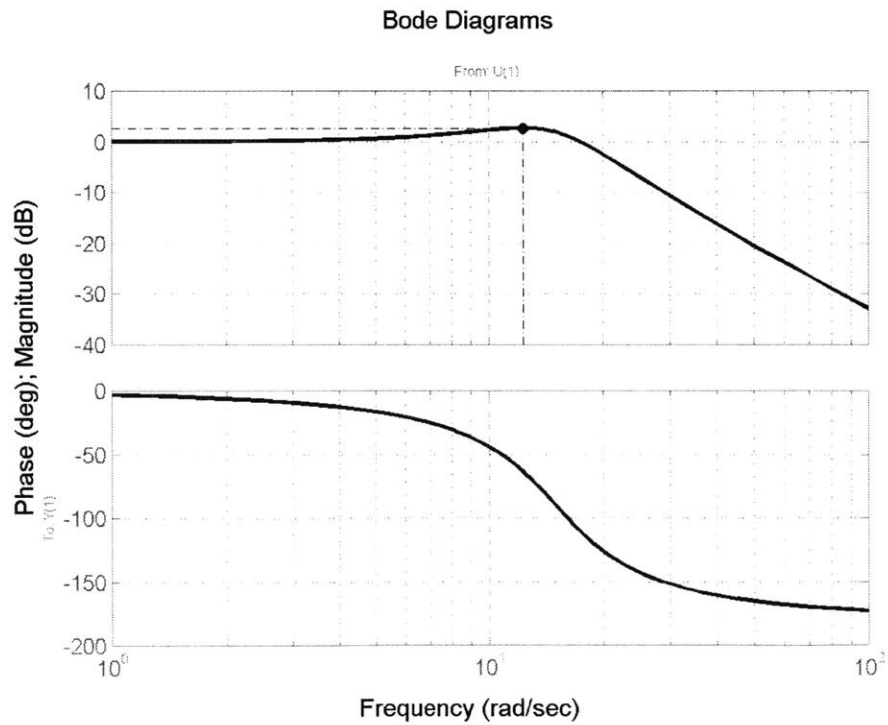
Bode Diagrams

Figure 5-8: Bode Diagram of Walker

5.4 Path Following

Although the walker has a vision system for closed loop control, the better the SmartWalker can follow a given path, the less frequent the vision code needs to be run, which in turn frees up valuable processor time. This experiment evaluates how well the SmartWalker can follow a given trajectory. The SmartWalker is commanded to follow a path of approximately fifteen meters with five 90-degree corners. Note that the vision system sometimes misfires, resulting in the large gaps between readings. This is why the SmartWalker does not appear to return to its starting position. However, the SmartWalker regularly returned to its starting position within approximately 15 – 20 cm.
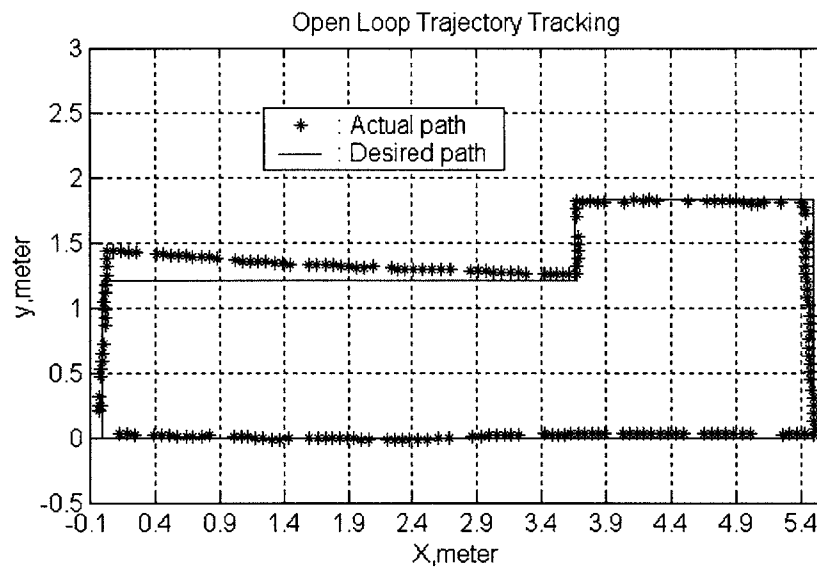
Figure 5-9: SmartWalker Following a Path

5.5 Conclusions

Several experiments were performed on the SmartWalker in an attempt to characterize the system and record its performance. These experiments included:

- determining the power consumption
- showing the motor step response
- showing the SmartWalker's step response
- finding an approximate transfer function of the SmartWalker.

- Determining the accuracy of the SmartWalker's open loop path following capabilities.

The results showed that it is possible for an elderly person to run the SmartWalker for one day before recharging the batteries. The experiments also showed that motor step response was adequate and could be tuned if necessary. Furthermore, the experiments indicated that the SmartWalker has a natural frequency of approximately 15 Hz. Finally, the experiments demonstrated that the SmartWalker's omnidirectional platform had excellent path following capabilities.

Chapter

6

Conclusion

6.1 Contributions

This thesis outlines the steps necessary to bring to realization the concept of the SmartWalker. The main contributions are outlined below.

6.1.1 Omnidirectional Platform

It was shown that all of the wheels of the SmartWalker's omnidirectional platform maintain contact with the floor at all times. It was also shown, through a simulation, that the SmartWalker's motion control algorithms, which were designed for a flat floor, will suffice for an uneven floor.

6.1.2 Stability

Three different analyses were performed in order to verify that the SmartWalker would be stable. It was shown that under normal conditions, the SmartWalker would not slip, tip over, or experience brake failure.

6.1.3 Mechanical Design

The mechanical design decisions and their justifications were presented. Most of the design decisions focused on the tradeoff between strength and weight. Other important and interesting designs were the layout of the SCMMs and the design of slip rings.

6.1.4 Experimental Results

The experiments showed that the SmartWalker should be able to be used by an elderly person for an entire day without the batteries needing to be recharged. Furthermore, it was shown that the motor step response was adequate, the SmartWalker has a natural frequency of about 15 Hz, and that the omnidirectional platform can closely follow a given path.

6.2 Suggested Further Work

As when building anything for the first time, one easily finds simpler and easier designs for future revisions. There are several modifications to parts that could be made to make the design more robust and easier to manufacture. One example is that the slip ring's design needs to be refined in order to reduce the errors that were discussed in Section 4.3. In addition to further design refinements, work needs to be done integrating the user and the machine, including testing at an eldercare facility.

Works Cited

Bachman, G. "An Experimental Investigation of the COBOT Wheel Contact Patch." Diss. Department of Mechanical Engineering. Northwestern University, 1997.

Baltus, G., et al. "Towards Personal Service Robots for the Elderly." Dept. of CS and Robotics, CMU. <http://www.cs.cmu.edu/~nursebot/web/papers.html>

Barton, L. J. "A Shoulder to Lean on: Assisted Living in the U.S." American Demographics, 1997.

Beer, F., and Johnston, E. R. Mechanics of Materials. McGraw-Hill, 1992.

Darrigo, C. "Health Monitoring Sensors for a Personal Mobility Aid for the Elderly." Diss. Department of Mechanical Engineering. Massachusetts Institute of Technology, 2001.

Dubowsky S., et al. "PAMM - A Robotic Aid to the Elderly for Mobility Assistance and Monitoring: A 'Helping-Hand' for the Elderly." Proceedings of IEEE International Conference on Robotics and Automation 1 (2000): 570-6.

Edwards, C.H. Jr., Penney, D. E. Calculus with Analytical Geometry. Englewood Cliffs, New Jersey: Prentice Hall, 1994.

Ferriere, L., and Raucent, B. "ROLLMOBS, a New Universal Wheel Concept." Proceedings of the IEEE International Conference on Robotics and Automation (1998): 1877-82.

Finkel, J., Fernie, G., and Cleghorn, W. "A Guideline for the Design of a Four-Wheeled Walker." RESNA Assistive Technology 9 (1997): 116-29.

Gabrel, C. S. "Characteristics of Elderly Nursing Home Current Residents and Discharges: Data from the 1997 National Nursing Home Survey." Advance Data from Vital and Health Statistics of the Centers for Disease Control and Prevention/National Center for Health Statistics 312 (2000).

Godding, S. "Field Tests on a Personal Mobility Aid for the Elderly." Diss. Department of Mechanical Engineering. Massachusetts Institute of Technology, 1999.

Kozono, H. SmartWalker Electronics and Computer Manual. Field and Space Robotics Lab, Department of Mechanical Engineering. Massachusetts Institute of Technology, 2000.

Lacey, G., and Dawson-Howe, K. M. "The Application of Robotics to a Mobility Aid for the Elderly Blind." Robotics and Autonomous Systems 23 (1998): 245-52.

Maxon Motor AG. Main Catalogue. Brünigstrasse 220, P.O. Box 263, CH-6072 Sachslen, 1999.

Miyawki, K., et al. "Development of Drived Cart for Assisting Biped-Locomotion of Elder People [sic]." Proceedings of the JSME Joint Symposium of Sports Engineering and Human Dynamics 97.34 (1997): 209-12.

Mori, H. and Kotani, S. "A Robotic Travel Aid for the Blind – Attention and Custom for Safe Behavior." Eighth International Symposium on Robotics Research Springer-Verlag, London (1998): 237-245.

Muir, P.F., and Neuman, C.P. "Kinematic Modeling for Feedback Control of an Omni-directional Wheeled Mobile Robot." Proceedings of IEEE International Conference on Robotics and Automation (1987): 1772-8.

Nemoto, Y., et al. "Power-Assisted Walking Support System for Elderly." Proceedings of the 20th Annual International Conference of the IEEE Engineering in Medicine and Biology Society 5 (1998): 2693-5.

Papadopoulos, E.G., and Rey, D.A. "A New Measure of Tipover Stability Margin for Mobile Manipulators." Proceedings of the 1996 IEEE International Conference on Robotics and Automation 4 (1996): 3111-6.

Rexroth Star 14001 South Lakes Dr. Charlotte, NC 2827

Schneider, E. L. "Aging in the Third Millennium." Science 283.54003 (1999): 796-7.

Schraft, R.D., Schaeffer, C., and May, T. "Care-O-bot™: the Concept of a System for Assisting Elderly or Disabled Persons in Home Environments." Proceedings of the 24th Annual Conference of the IEEE Industrial Electronics Society 4 (1998): 2476-81.

Shigley, J.E., and Mischke, C.R. Mechanical Engineering Design. McGraw-Hill, 1989.

Simeon, T., Dacre-Wright, B. "A Practical Motion Planner for All-terrain Mobile Robots." Proceedings of the 1993 IEEE/RSJ International Conference on Intelligent Robots and Systems 2 (1993): 1357-63.

Tal, J. "Design and Analysis of Pulsewidth-Modultated Amplifiers for DC Servo Systems." IEEE Transactions on Industrial Electronics and Control Instrumentation 23.1 (1976): 47-55.

Walk Easy, Inc. 2915 S. Congress Ave. Delray Beach, FL 33445

West, M., and Asada, H. "Design of Ball Wheel Mechanisms for Omnidirectional Vehicles with Full Mobility and Invariant Kinematics," Journal of Mechanical Design 119 (1997): 153-161.

Yu, H., Dubowsky, S., and Skwersky, A., "Omni-directional Mobility Using Active Split Offset Castors," Proceedings of 2000 ASME IDETC/CIE 26th Biennial Mechanics and Robotics Conference September 10-13, 2000, Baltimore, Maryland.

Appendix

A

Analysis of a SCMM Traversing Uneven Terrain

This appendix contains the details of the simulation described in Chapter 2. The appendix follows the tasks outlined in Figure 2-18. Refer to Figure 2-13 and Figure 2-14 for notation and explanation of any symbols.

The controller's only input is Ψ, the angle of the offset link to the encoder shaft. The controller gives the following velocity commands to wheels two and one, respectively.

$$V_2 = \left(\cos\psi + \frac{d}{2s}\sin\psi \right)V_X + \left(\sin\psi - \frac{d}{2s}\cos\psi \right)V_Y \tag{A-1}$$

$$V_1 = \frac{V_X - \left(\left(\frac{1}{2}\cos\psi + \frac{s}{d}\sin\psi \right)V_2 \right)}{\frac{1}{2}\cos\psi - \frac{s}{d}\sin\psi} \tag{A-2}$$

where V_X and V_Y are the desired velocities of point D, s is the length of the offset and d is the length of the split. The velocity of point D is determined using Equation (2-20). The position of point D is then calculated using:

$$\mathbf{D} = \mathbf{D}(t-1) + \mathbf{V}_D * dt \tag{A-3}$$

where $\mathbf{D}$(t-1) is the previous position of point D, $\mathbf{V}_D$ is the velocity of point D, and dt is the time step.

The position of point D is then transformed into the body reference coordinates, **uwz**, using:

$$\begin{bmatrix} D_u \\ D_w \\ D_z \end{bmatrix} = \begin{bmatrix} \cos\psi & \sin\psi & 0 \\ -\cos\theta\sin\psi & \cos\theta\cos\psi & \sin\theta \\ \sin\theta\sin\psi & -\sin\theta\cos\psi & \cos\theta \end{bmatrix} \begin{bmatrix} D_X \\ D_Y \\ D_Z \end{bmatrix} \qquad \text{(A-4)}$$

The location of point C is then determined using:

$$\begin{bmatrix} C_u \\ C_w \\ C_z \end{bmatrix} = \begin{bmatrix} D_u \\ D_w - l\sin\theta \\ D_z - l\cos\theta \end{bmatrix} \qquad \text{(A-5)}$$

where 1 is the length of the encoder shaft. The position of point C then needs to be converted into **XYZ** coordinates. This is done using the following equation:

$$\begin{bmatrix} C_X \\ C_Y \\ C_Z \end{bmatrix} = \begin{bmatrix} \cos\psi & -\sin\psi\cos\theta & \sin\theta\sin\psi \\ \sin\psi & \cos\theta\cos\psi & -\sin\theta\cos\psi \\ 0 & \sin\theta & \cos\theta \end{bmatrix} \begin{bmatrix} C_u \\ C_w \\ C_z \end{bmatrix} \qquad \text{(A-6)}$$

Now that the position of point C has been determined, the wheel contact points can be calculated using the following equations:

$$P_{wheel1} = \begin{bmatrix} C_X + \left(\dfrac{d}{2}\cos\theta\sin\Psi - (s - r\sin\gamma_1)\cos\Psi\right) \\ C_Y - \left((s - r\sin\gamma_2)\sin\Psi + \dfrac{d}{2}\cos\theta\cos\Psi\right) \\ f(x,y) \end{bmatrix} \qquad \text{(A-7)}$$

$$P_{wheel2} = \begin{bmatrix} C_X - \left(\dfrac{d}{2}\cos\theta\sin\Psi + (s - r\sin\gamma_1)\cos\Psi\right) \\ C_Y - \left((s - r\sin\gamma_2)\sin\Psi - \dfrac{d}{2}\cos\theta\cos\Psi\right) \\ f(x,y) \end{bmatrix} \qquad \text{(A-8)}$$

where f(x,y) is the function that describes the floor and r is the radius of the wheels. From that point, the new values for γ, θ, and $\dot{\theta}$ need to be determined.

γ is the arctangent of the derivative of the function f(x,y) with respect to **u**. Thus, the function f(x,y) needs to be converted into f(u,w,z). First, expressions of x and y need

to be converted into expressions of u, w, and z using the relationships given in Equations (A-9) and (A-10).

$$x = \cos \Psi u + \sin \Theta \sin \Psi w + \sin \Theta \sin \Psi z \qquad \text{(A-9)}$$

$$y = \sin \Psi u + \cos \Theta \cos \Psi w - \sin \Theta \cos \Psi z \qquad \text{(A-10)}$$

Plugging these equations into (2-23) yields.

$$f(u,w,z) = amp(\exp(-(peak(\cos \Psi u + \sin \Theta \sin \Psi w + \sin \Theta \sin \Psi z))^2$$
$$- (peak(\sin \Psi u + \cos \Theta \cos \Psi w - \sin \Theta \cos \Psi z))^2)) \qquad \text{(A-11)}$$

Then the derivative needs to be taken with respect to u.

$$\frac{\partial f(u,w,z)}{\partial u} = amp(-2peak^2(\cos \Psi u + \sin \Theta \sin \Psi w + \sin \Theta \sin \Psi z)\cos \Psi$$

$$- 2peak^2(\sin \Psi u + \cos \Theta \cos \Psi w - \sin \Theta \cos \Psi z)\sin \Psi) \qquad \text{(A-12)}$$
$$(\exp(-(peak(\cos \Psi u + \sin \Theta \sin \Psi w + \sin \Theta \sin \Psi z))^2$$
$$- (peak(\sin \Psi u + \cos \Theta \cos \Psi w - \sin \Theta \cos \Psi z))^2))$$

After substituting back in for x and y, the equation simplifies to

$$\frac{\partial f(u,w,z)}{\partial u} = -2amp * peak^2 (x\cos \Psi - y\sin \Psi)\left(\exp\left(- (peak * x)^2 - (peak * y)^2\right)\right)$$

$$\text{(A-13)}$$

and thus,

$$\gamma = \tan^{-1}\left(\frac{\partial f(u,w,z)}{\partial u}\right)$$

$$= \tan^{-1}\left(- 2amp * peak^2 (x\cos \Psi - y\sin \Psi)\left(\exp\left(- (peak * x)^2 - (peak * y)^2\right)\right)\right)$$

$$\text{(A-14)}$$

where x and y are the positions of the wheel. Θ can be determined using:

$$\Theta = \sin\left(\frac{z_{wheel2} - z_{wheel1}}{d}\right) \qquad \text{(A-15)}$$

The time rate change of theta, $\dot{\theta}$, can be calculated using:

$$\dot{\theta} = \frac{\theta - \theta(t-1)}{dt} \qquad \text{(A-16)}$$

Finally, Ψ, is calculated using

$$\psi = \psi(t-1) + \left(\frac{s}{d}(V_1 - V_2) - \dot{\theta} * l * \sin\theta \right) \frac{\cos\theta}{s} dt \qquad \text{(A-17)}$$

These are the equations necessary to run the simulation presented in Chapter 2.

Appendix

B

Tipover Margin

This appendix details the derivation of the tipover stability measure that is used in this thesis. It is based on work done by (Papadopoulos, 1996). The benefits of this measure are that it is readily understood using graphical methods, easily computed, sensitive to topheaviness, and can be used for situations that have both internal and external forces.
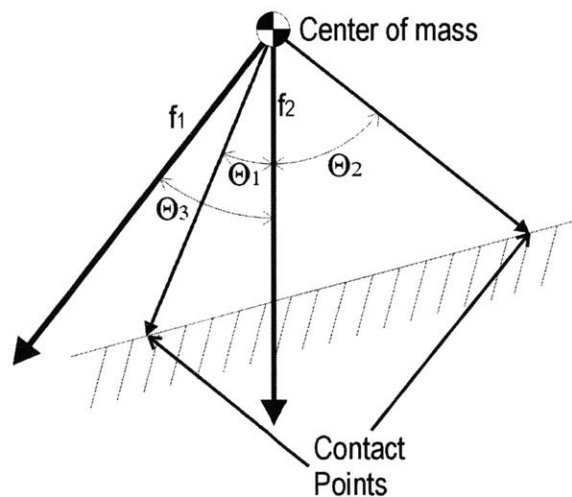

Figure B-1: 2-D Representation of Contact Polygon (Adapted from Papadopoulos, 1996)

The stability measure can be easily exemplified using a planar example (see Figure B-1). The center of mass is connected to each contact point by a line. If a force vector lies within the two lines, as does $\mathbf{f}_2$, then the system is stable. If the force vector lies outside of the two lines, as does $\mathbf{f}_1$, then the system is unstable. Note that as the center of mass is raised higher above the ground, the angle necessary to create instability

decreases. The following is the derivation of the stability measure, α, as described in Equation (3-5).

In a three-dimensional case, only the outermost ground contact points, or those that form a convex polygon, need to be considered. The ith ground contact points are represented by $\mathbf{p}_i$ such that:

$$\mathbf{p}_i = \begin{bmatrix} p_x & p_y & p_z \end{bmatrix}^T \qquad i = \{1,...,n\} \qquad \text{B-1}$$

The lines that form the support polygon, the candidate tipover axes, are labeled $\mathbf{a}_i$ and are defined by:

$$\mathbf{a}_i = (\mathbf{p}_{i+1} - \mathbf{p}_i) \qquad i = \{1,...,n-1\} \qquad \text{B-2}$$

$$\mathbf{a}_n = \mathbf{p}_1 - \mathbf{p}_n \qquad \text{B-3}$$

If $\hat{\mathbf{a}} = \dfrac{\mathbf{a}}{\|\mathbf{a}\|}$, and $\mathbf{p}_c$ is the center of mass, then the tipover axis normals, $\mathbf{l}$, are given by:

$$\mathbf{l}_i = (1 - \hat{\mathbf{a}}_i \hat{\mathbf{a}}_i^T)(\mathbf{p}_{i+1} - \mathbf{p}_c) \qquad \text{B-4}$$

For the case of the SmartWalker, the following force equilibrium equations apply.

$$\sum \mathbf{f}_{inertial} = \sum \left(\mathbf{f}_{grav} + \mathbf{f}_{manip} + \mathbf{f}_{support} \right) \qquad \text{B-5}$$

where $\mathbf{f}_{grav}$ is the gravitational load, $\mathbf{f}_{manip}$ is the load seen by the force/torque sensor, and $\mathbf{f}_{support}$ are the reaction forces acting on the wheels by the ground. The net force acting on the center of mass is:

$$\begin{aligned} \mathbf{f}_r &\equiv \sum \left(\mathbf{f}_{grav} + \mathbf{f}_{manip} - \mathbf{f}_{inertial} \right) \\ &= -\sum \mathbf{f}_{support} \end{aligned} \qquad \text{B-6}$$

The net moment acting about the center of mass is:

$$\begin{aligned} \mathbf{n}_r &\equiv \sum \left(\mathbf{n}_{grav} + \mathbf{n}_{manip} - \mathbf{n}_{inertial} \right) \\ &= -\sum \mathbf{n}_{support} \end{aligned} \qquad \text{B-7}$$

Only the components of $\mathbf{f}_r$ and $\mathbf{n}_r$ that act on the tipover axis need to be considered.

Thus for each tipover axis i, define

$$\mathbf{f}_i = \left(1 - \hat{\mathbf{a}}_i \hat{\mathbf{a}}_i^T\right) \mathbf{f}_r$$
$$\mathbf{n}_i = \left(\hat{\mathbf{a}}_i \hat{\mathbf{a}}_i^T\right) \mathbf{n}_r$$

B-8

The moment $\mathbf{n}_i$ must be replaced with an equivalent force couple $\mathbf{f}_{ni}$ for each of the tipover axes. The part of the moment that acts on the center of mass is given by the following:

$$\mathbf{f}_{ni} = \frac{\hat{\mathbf{l}}_i \times \mathbf{n}_i}{\|\mathbf{l}_i\|}$$

B-9

where $\hat{\mathbf{l}} = \dfrac{\mathbf{l}}{\|\mathbf{l}\|}$. This means that $\mathbf{f}_i^*$, the new net force vector for the ith tipover axis, becomes

$$\mathbf{f}_i^* = \mathbf{f}_i + \frac{\hat{\mathbf{l}}_i \times \mathbf{n}_i}{\|\mathbf{l}_i\|}$$

B-10

where $\hat{\mathbf{f}}^* = \dfrac{\mathbf{f}^*}{\|\mathbf{f}^*\|}$. The candidates for the tipover are given by

$$\Theta_i = \sigma_i \cos^{-1}\left(\hat{\mathbf{f}}^* \cdot \hat{\mathbf{l}}_i\right)$$

B-11

where $-\pi \leq \Theta_i \leq \pi$. The sign of Θ is determined by the following equation:

$$\sigma i = \begin{cases} +1 & \left(\hat{\mathbf{l}}i \times \hat{\mathbf{f}}_i^*\right) \cdot \hat{\mathbf{a}}_i < 0 \\ -1 & otherwise \end{cases}$$

B-12

Thus, the force stability measure is given by:

$$\alpha = \min\left(\theta_i\right)\|fr\| \quad i = \{1,...,n\}$$

B-13